Research Square

Preprints are preliminary reports that have not undergone peer review.
They should not be considered conclusive, used to inform clinical practice,
or referenced by the media as validated information.

Visible lighted assisted magnetic COF/HKUST/CoFe2O4 composite as a novel photocatalyst: Green synthesis and efficient degradation of pollutants (dye and pharmaceutical) in water

Bahareh Rabeie
Institute for Color Science and Technology
Niyaz Mohammad Mahmoodi
nm_mahmoodi@aut.ac.ir

Institute for Color Science and Technology
Hossein Kazemian
University of Northern British Columbia (UNBC)

Research Article

Keywords: Green synthesis, Magnetic COF/HKUST/CoFe2O4 composite, Photocatalysis, Dye and pharmaceutical degradation, Water

Posted Date: December 17th, 2025

DOI: https://doi.org/10.21203/rs.3.rs-8196220/v1

License: This work is licensed under a Creative Commons Attribution 4.0 International License.
Read Full License

Additional Declarations: No competing interests reported.

Version of Record: A version of this preprint was published at Advanced Composites and Hybrid Materials on March 11th, 2026. See the published version at https://doi.org/10.1007/s42114-026-01696-9.

Visible lighted assisted magnetic COF/HKUST/$CoFe_2O_4$ composite as a novel photocatalyst: Green synthesis and efficient degradation of pollutants (dye and pharmaceutical) in water

Bahareh Rabeie [a], Niyaz Mohammad Mahmoodi [a*], Hossein Kazemian [b]

[a] Department of Environmental Research, Institute for Color Science and Technology, Tehran, Iran

[b] Northern Analytical Laboratory Service (NALS), University of Northern British Columbia (UNBC), Prince George, BC, Canada

[*]Corresponding author (Prof. Dr. N.M. Mahmoodi)

E-mail addresses:

mahmoodi@icrc.ac.ir; nm_mahmoodi@aut.ac.ir (Prof. Dr. N.M. Mahmoodi)

Rabeie-ba@icrc.ac.ir; b_rabeie@yahoo.com (Dr. B. Rabeie)

Abstract

This study reports the facile, green synthesis of ternary magnetic photocatalyst composites (COF/HKUST/$CoFe_2O_4$) with tunable COF: HKUST ratios, integrating an amide-based covalent organic framework, the metal-organic framework (HKUST-1), and $CoFe_2O_4$ nanoparticles. The hybrid was comprehensively characterized by FTIR, XRD, SEM, MAP and EDX, TEM, VSM, AFM, PL and DRS. The optimized COF/HKUST/$CoFe_2O_4$ composite achieved 95% degradation of 90 mg/L doxycycline (DOX) within 180 min and 97% removal of 20 mg/L methylene blue (MB) in 150 min under visible-light irradiation. This efficacy stems from synergistic heterointerface interactions that promote efficient charge separation, accelerated electron transfer, and suppressed recombination. Kinetic modeling confirmed second-order degradation for DOX and first-order for MB, while scavenging assays identified photogenerated holes (h^+) as the dominant oxidative species, followed by hydroxyl radicals (•OH) and superoxide anions ($•O_2^-$). Notably, the composite enables straightforward magnetic separation, and robust recyclability, retaining >72% pollutant degradation efficiency over five consecutive cycles. This work advances sustainable wastewater remediation by providing a low-cost, scalable photocatalyst that aligns with circular economy principles and United Nations Sustainable Development Goal 6, offering a versatile platform for mitigating antibiotic resistance and dye-induced aquatic toxicity.

Keywords: Green synthesis; Magnetic COF/HKUST/$CoFe_2O_4$ composite; Photocatalysis; Dye and pharmaceutical degradation; Water

1. Introduction

The escalating water shortage crisis, exacerbated by uneven regional [1], and severe pollution from industrialization, has discharged toxic, carcinogenic, and genotoxic substances into aquatic systems. These contaminants impair human health, marine ecosystems, and biodiversity,

Compounding this, dwindling fossil fuel reserves necessitate a shift to sustainable energy sources [2]. Solar energy stands out for its cleanliness and inexhaustibility, powering applications like photovoltaics, CO_2 photoreduction [3], nitrogen fixation [3], the degradation of organic compounds [4,5], and photocatalytic water splitting [6]. Photocatalysis excels with strong redox capabilities, cost-effectiveness, minimal secondary pollution, and reliance on abundant sunlight, positioning it as a cornerstone for environmental remediation. Yet, to achieve economic viability and sustainability, innovative, efficient, non-toxic photocatalysts are essential [7].

Among persistent pollutants, antibiotics—stemming from pharmaceutical plants, aquaculture, and hospitals pose acute risks. Retained biological activity in effluents fosters antibiotic resistant bacteria and genes, with bioaccumulation in water threatening ecosystems and public health [8,9]. Doxycycline (DOX), a broad-spectrum tetracycline, exemplifies this peril, persisting in waterways and disrupting microbial communities. Similarly, methylene blue (MB), a phenothiazine dye with redox properties used in textiles and medicine, degrades water aesthetics, induces aquatic toxicity, and causes human respiratory and neurological issues upon exposure [10].

Recent breakthroughs in porous organic polymers, particularly covalent organic frameworks (COFs) and metal-organic frameworks (MOFs), have revolutionized catalysis. Their high surface areas, tunable pores, and modular designs enhance reaction rates and selectivity, enabling multifunctional platforms with diverse chemistries [11–13].

Unlike amorphous polymers, crystalline organic frameworks allow precise control over morphology, pore size, and dimensions, leveraging abundant organic building blocks for advanced structural and functional tailoring [14,15].

To boost photocatalytic performance, heterogeneous junctions integrating COFs/MOFs with semiconductors facilitate charge separation and broaden light absorption [16,17]. Hybrids of organic frameworks with ferrites have garnered attention for pollutant abatement [18–20]. Notably, ferrite nanostructures (e.g., $CoFe_2O_4$) impart magnetic recoverability, tunable bandgaps for visible-light harvesting, and suppressed electron-hole recombination, streamlining reuse and cost-efficiency [23–27].

Despite these advances, no prior studies have explored COF/HKUST (Cu-based MOF)/$CoFe_2O_4$ composites for DOX and MB degradation. Herein, we report the facile and green synthesis of magnetic photocatalyst variants (COF/HKUST/$CoFe_2O_4$) at varying ratios of (COF: HKUST), integrating porosity of COF, coordination sites of HKUST, and magnetism of $CoFe_2O_4$. Materials including pristine COF, HKUST, $CoFe_2O_4$, and COF/HKUST/$CoFe_2O_4$ were characterized via FTIR, XRD, SEM, EDX mapping, TEM, VSM, AFM, and DRS. Optimal composites achieved superior degradation of DOX and MB under visible light, with parameter optimization (concentration, dosage, etc.) revealing key influences. Mechanismic insights, informed by scavenging tests and band alignments, highlight reactive species roles. Reusability (5 cycles) and stability underscore practical viability.

2. Experimental

2.1. Materials

The used materials were inserted in Table 1.

Table 1. Information of the raw materials utilized

Name	Molecular Formula	Molecular Weight (g/mol)	Purity	Company
Melamine	$C_3H_6N_6$	126.12	≥ 99	Sigma-Aldrich
1,3,5-benzenetricarboxylic acid	$C_9H_6O_6$	210.14	≥ 99	Sigma-Aldrich
Copper(II) nitrate Trihydrate	$Cu(NO_3)_2 \cdot 3H_2O$	241.6	≥ 99.5	Merck
Iron(III) nitrate nonahydrate	$Fe(NO_3)_3 \cdot 9H_2O$	404.00	≥ 98	Merck
Cobalt(III) nitrate nonahydrate	$Co(NO_3)_3 \cdot 9H_2O$	407.08	≥ 99	Merck
Sodium hydroxide	NaOH	39.99	≥ 99	Merck
ethyl alcohol	EtOH	46.07	≥ 99.9	Merck

2.2. Catalyst synthesis

2.2.1. COF

Fig. 1 shows the COF preparation. Initially 5 mmol of melamine was dispersed in 50 mL of water utilizing a magnetic stirrer. Subsequently, 7.5 mmol of benzene tricarboxylic acid was introduced into the suspension. The resultant mixture was continuously agitated at ambient temperature. A white precipitate formed, which was then harvested using filter paper. This precipitate was subsequently rinsed multiple times with water and ethanol. Ultimately, it was subjected to drying in an oven at 70 °C for a duration of 8 h [24–26].

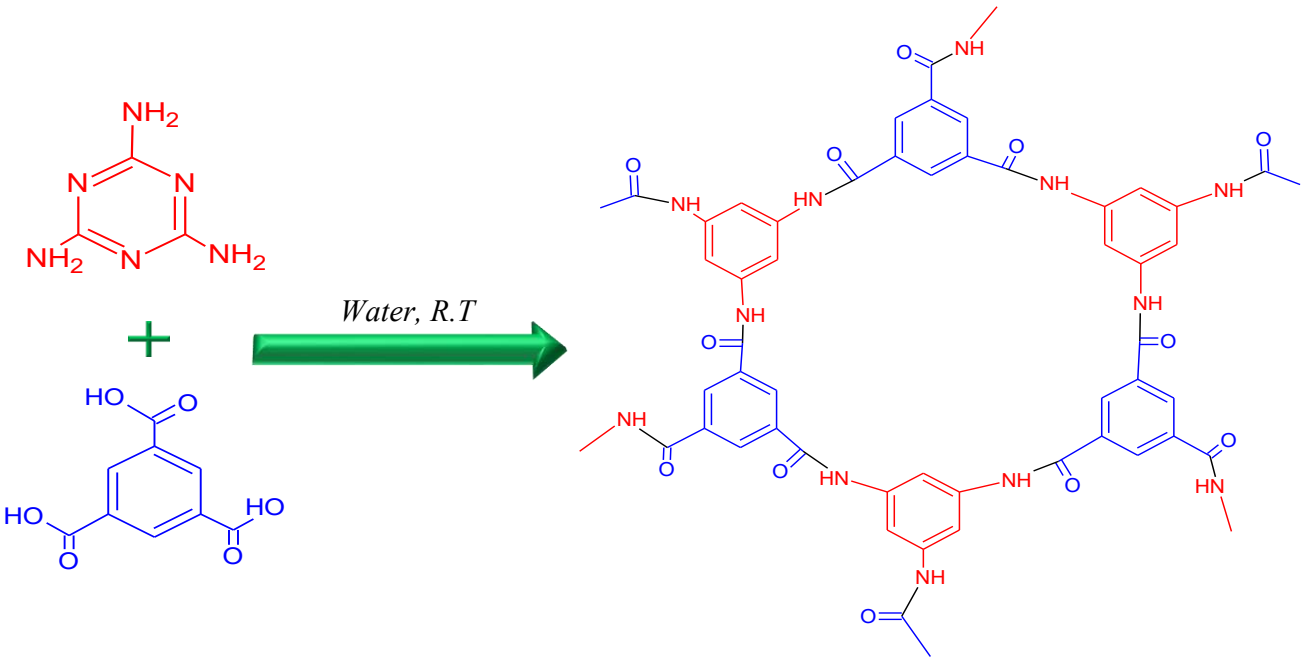


Fig. 1. Chemical synthesis of COF

2.2.2. HKUST

Fig. 2 shows the HKUST preparation. $Cu(NO_3)_2 \cdot 3H_2O$ (3.6 mmol) was poured in water (12 mL). Concurrently, 1,3,5-benzenetricarboxylic acid (2.0 mmol) was added to ethanol (12 mL). The trimesic acid solution was then added. The resultant mixture was heated at 120°C for 12 h [27]. The product was washed in water then ethanol and dried. Fig. 3 presents the image of the synthesized HKUST.

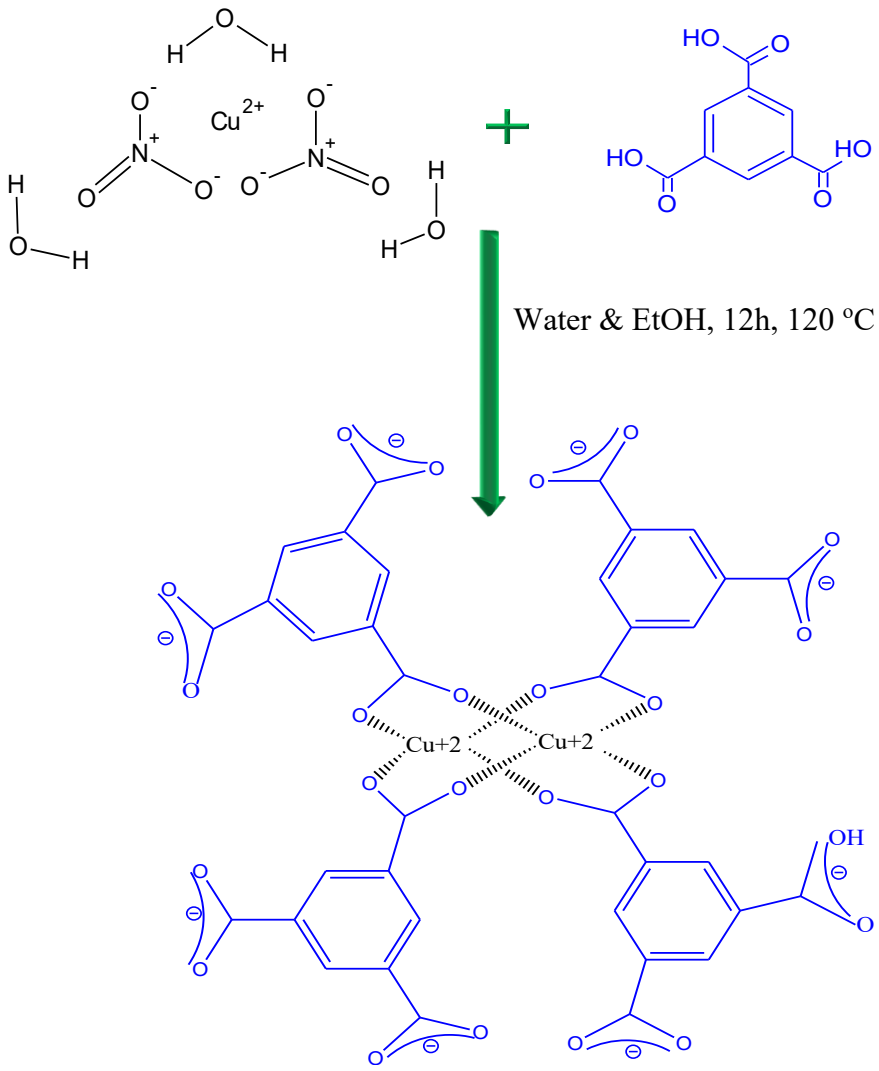


Fig. 2. The synthesis procedure of HKUST.

2.2.3. $CoFe_2O_4$

A total of 10 mmol of $Fe(NO_3)_3 \cdot 9H_2O$ was meticulously dissolved in water (70 mL), followed by the incremental addition of 4.35 mmol of $Co(NO_3)_3 \cdot 9H_2O$, yielding a clear solution. The 1 M NaOH solution was then introduced gradually to this solution, with continuous stirring at ambient temperature for an additional duration of 6 h. Subsequently, the mixture was transferred to an autoclave and subjected to thermal treatment at 180°C for 12 h. The resulting precipitate was

thoroughly washed twice with water, then with ethanol, and finally with acetone. The precipitate was subsequently dried in an oven at 80°C overnight [28].

2.2.4. Binary COF/HKUST composite

Melamine (1.5 mmol) was dispersed in 50 mL of deionized water. Trimesic acid (4 mmol) was then added under magnetic stirring, and the mixture was stirred for 2 h, resulting in the formation of a bulky white precipitate. Subsequently, 3.6 mmol of $Cu(NO_3)_2 \cdot 3H_2O$ was added, followed by 2.0 mmol of trimesic acid dissolved in ethanol. The mixture was stirred for an additional 2 h at room temperature, then transferred to an autoclave and heated at 120°C for 12 h. The resulting turquoise precipitate was washed in water then ethanol, and dried, yielding the binary COF/HKUST-1 composite. Fig. 3 presents the image of the synthesized COF/HKUST.

2.2.5. Ternary COF/HKUST/$CoFe_2O_4$ composite

All steps for the preparation of COF/HKUST/$CoFe_2O_4$ are schematically represented in Fig. 4. Melamine (1.5, 3, and 6 mmol) was dispersed in 50 mL of deionized water. Subsequently, trimesic acid (4, 5.5, and 8.5 mmol) was added using a magnetic stirrer, and the mixture was stirred for 2 h until a bulky white precipitate appeared. Next, 0.5 g of PVP and 0.05 g of cobalt ferrite were introduced into the reaction mixture. In the following step, $Cu(NO_3)_2 \cdot 3H_2O$ (3.6 mmol), and trimesic acid (2.0 mmol) which dissolved in ethanol were added. After stirring the mixture for another 2 h at room temperature, it was transferred to an autoclave and maintained at 120°C for 12 h. The resulting gray turquoise precipitate was washed in water then ethanol, and dried. They labeled as COF /HKUST/$CoFe_2O_4$ -1, COF/HKUST/$CoFe_2O_4$ -2, and COF/HKUST/$CoFe_2O_4$-3, based on higher COF content respectively. Fig. 3 indicated the image of the synthesized composites.



Fig. 3. The images of (a) Magnet, (b) COF, (c) HKUST, (d) COF/HKUST binary composite, (e) COF/HKUST/$CoFe_2O_4$-1, (f) COF/HKUST/$CoFe_2O_4$-2, (g) COF/HKUST/$CoFe_2O_4$-3 ternary composite, and (h) $CoFe_2O_4$.

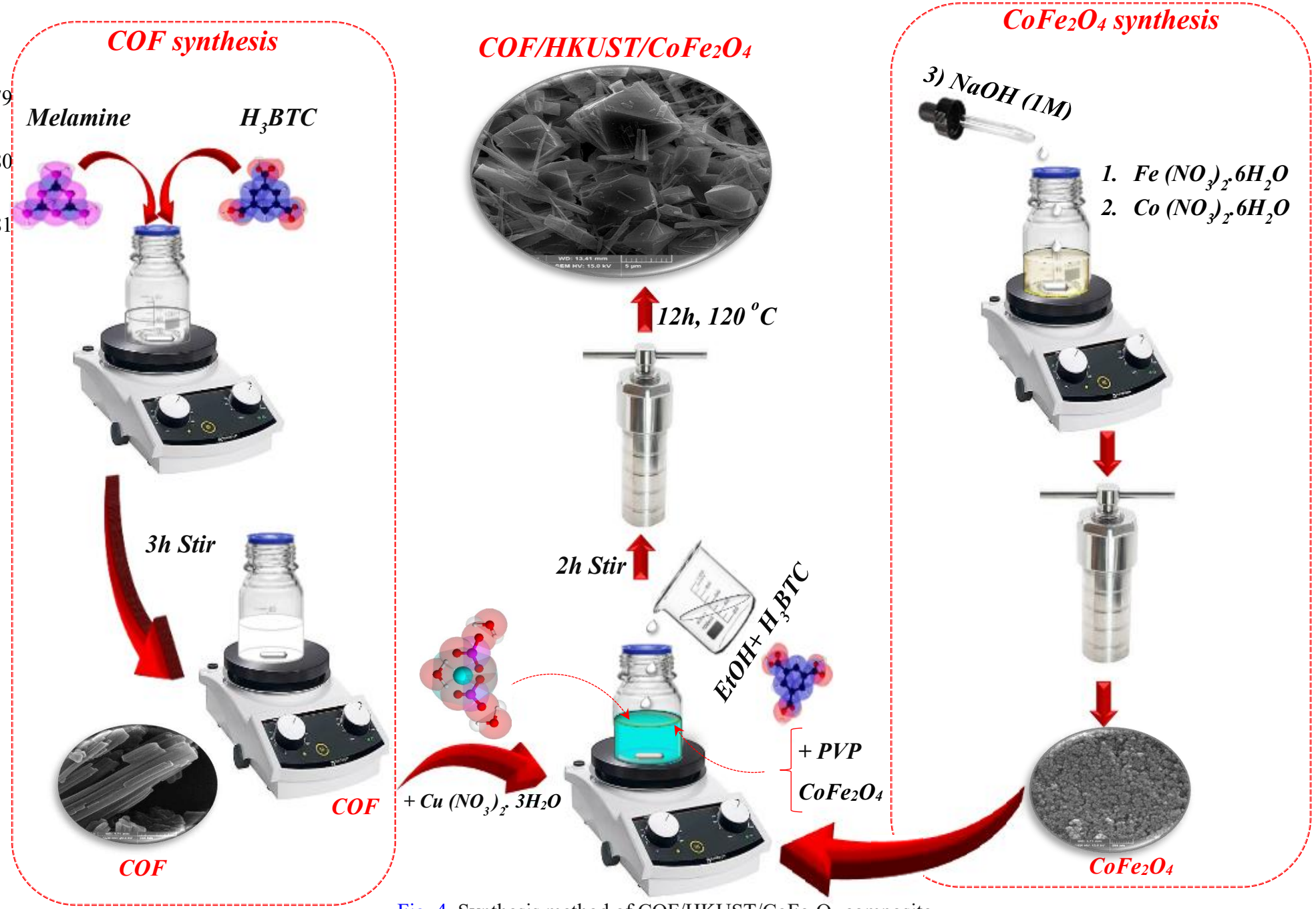


Fig. 4. Synthesis method of COF/HKUST/$CoFe_2O_4$ composite

2.3. Apparatus

This section is provided in the support file.

2.4. Contaminant removal

The photocatalytic efficiency of the ternary composite in degrading MB and DOX under visible light at room temperature and natural pH was assessed. During the experiment, 100 mL of the pollutant solution (MB and DOX) was mixed with a specific amount of catalyst and stirred magnetically for 60 minutes in darkness to attain adsorption-desorption equilibrium. 20 µL of hydrogen peroxide was added to the pollutant solution as the lamp was turned on, and samples of 3 ml were collected at specified time intervals. The samples were centrifuged at 6000 rpm for 5 minutes to separate the catalyst by Universal 320 instrument. The pollutant degradation rate was then assessed. The total experiment duration, including the adsorption-desorption equilibrium, was 210 minutes for methylene blue and 240 minutes for doxycycline.

3. Results and Discussion

3.1. Characterization

3.1.1. FTIR

Fig. 5 presents FTIR spectra of the synthesized materials. The pronounced peak observed at 579 cm^{-1} corresponds to the vibrations of metal-oxygen bonds. It highlights the stretching modes of Co-O and Fe-O bonds, thereby confirming the existence of both cobalt and iron within the spinel configuration of $CoFe_2O_4$. The peak in the range of 3400-3500 cm^{-1} is associated with O-H stretching vibrations. This spectral feature frequently suggests the existence of hydroxyl groups on the nanoparticle surface, another peak at 1620 cm^{-1} corresponds to H-O-H bending vibrations,

which may result from the adsorption of residual water molecules or moisture due to synthesis conditions. The peak at 1380 cm^{-1} may indicate metal-oxygen stretching or overlapping vibrational modes, depending on the synthesis method and specific conditions [29–31].

The prominent absorption at 3380 cm^{-1} is related to the stretching vibrations of –OH groups from water molecules found within the pores of HKUST. The peak observed at 1705 cm^{-1} corresponds to the stretching vibration of C=O in the linker. Meanwhile, the peak at 1368 cm^{-1} is associated with the stretching vibrations of C=C bonds, indicating the presence of aromatic components in the linker structure. The peak at 729 cm^{-1} is related to the scissoring vibration of a carboxylate ion (Cu-O). The carboxylate groups for forming coordination bonds with copper ions is used, which emphasizing the connectivity within the metal-organic framework (MOF) structure [32,33].

The peak at 1674 cm^{-1} indicates the presence of carbonyl groups typical of amides, confirming their integration into the COF structure. The peak at 1650 cm^{-1} likely corresponds to C-N bond stretching vibrations, characteristic of secondary amides due to the interaction of C-N and C=O functionalities in the covalent framework. The peak at 933 cm^{-1} can be attributed to out-of-plane bending or in-plane stretching of C-C bonds in the organic framework, reflecting the interconnected carbon structure vital for COF stability and function. Additionally, the absorption at 3110 cm^{-1} suggests C-H bond stretching, while the peak at 3397 cm^{-1} is related to N-H stretching vibrations in the amide groups [34–36].

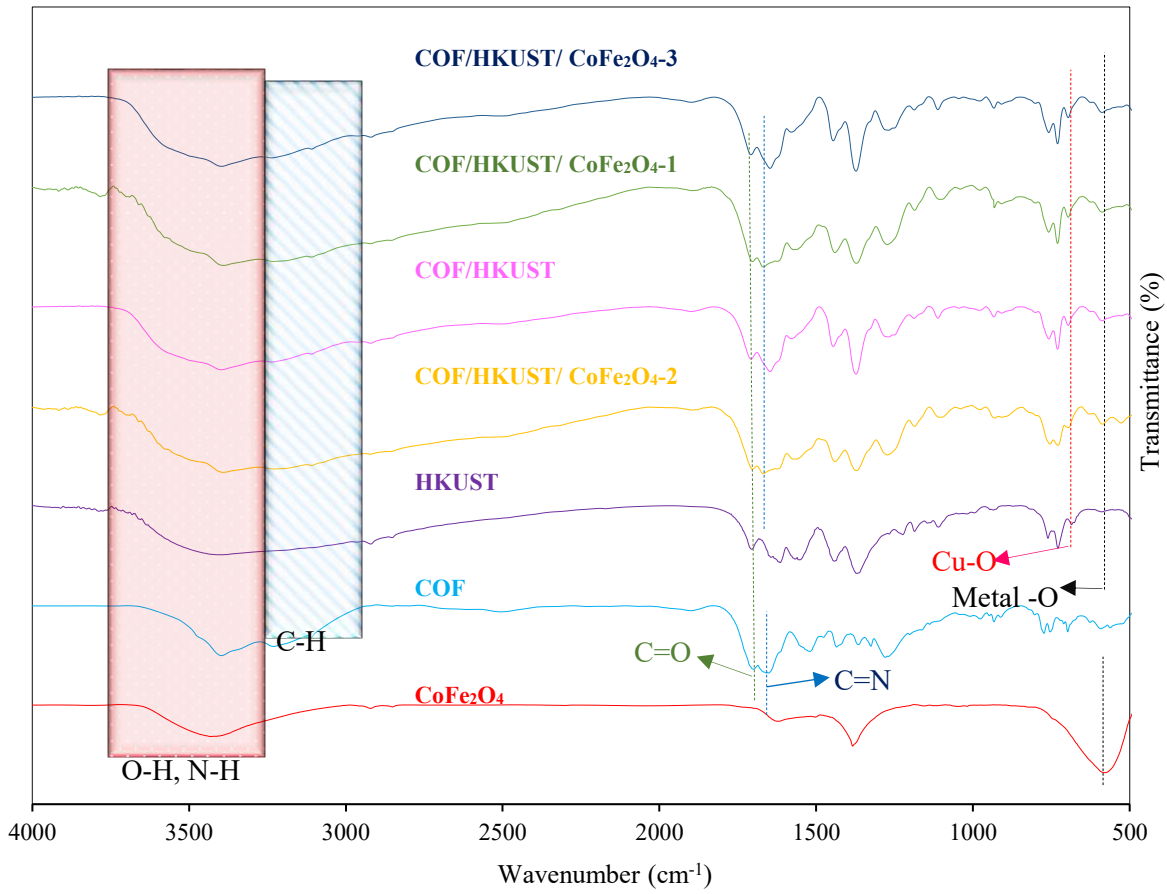


Fig. 5. FTIR spectra of the synthesized materials.

3.1.2. XRD

Fig. 6 reveals XRD patterns of the synthesized materials. The analysis of $CoFe_2O_4$ shows peaks at 19° (111), 30.22° (220), 35.52° (311), 43.23° (400), 53.7° (422), 57.15° (511), and 62.72° (440) [37,38]. The diffraction peaks observed at 2θ = 7.3° (200), 9.4° (220), 12.2° (222), 13.9° (400), 14.9° (331), 15.4° (420), 17.2° (422), 18.0° (333), 19.5° (440), 20.5° (600), 22.9° (444), 24.2° (551), 26.1° (533), 28.9° (555), 33.9° (860), and 38.8° (882) provide compelling evidence for the crystallization of HKUST, with all crystal planes distinctly identifiable [39,40]. The analysis of the polyamide COF reveals crystalline plateaus at diffraction angles of 2θ = 9.136, 10.756, 13.490,

18.502, 25.337, 27.616. These peaks suggest a high degree of order within the framework structure [26].

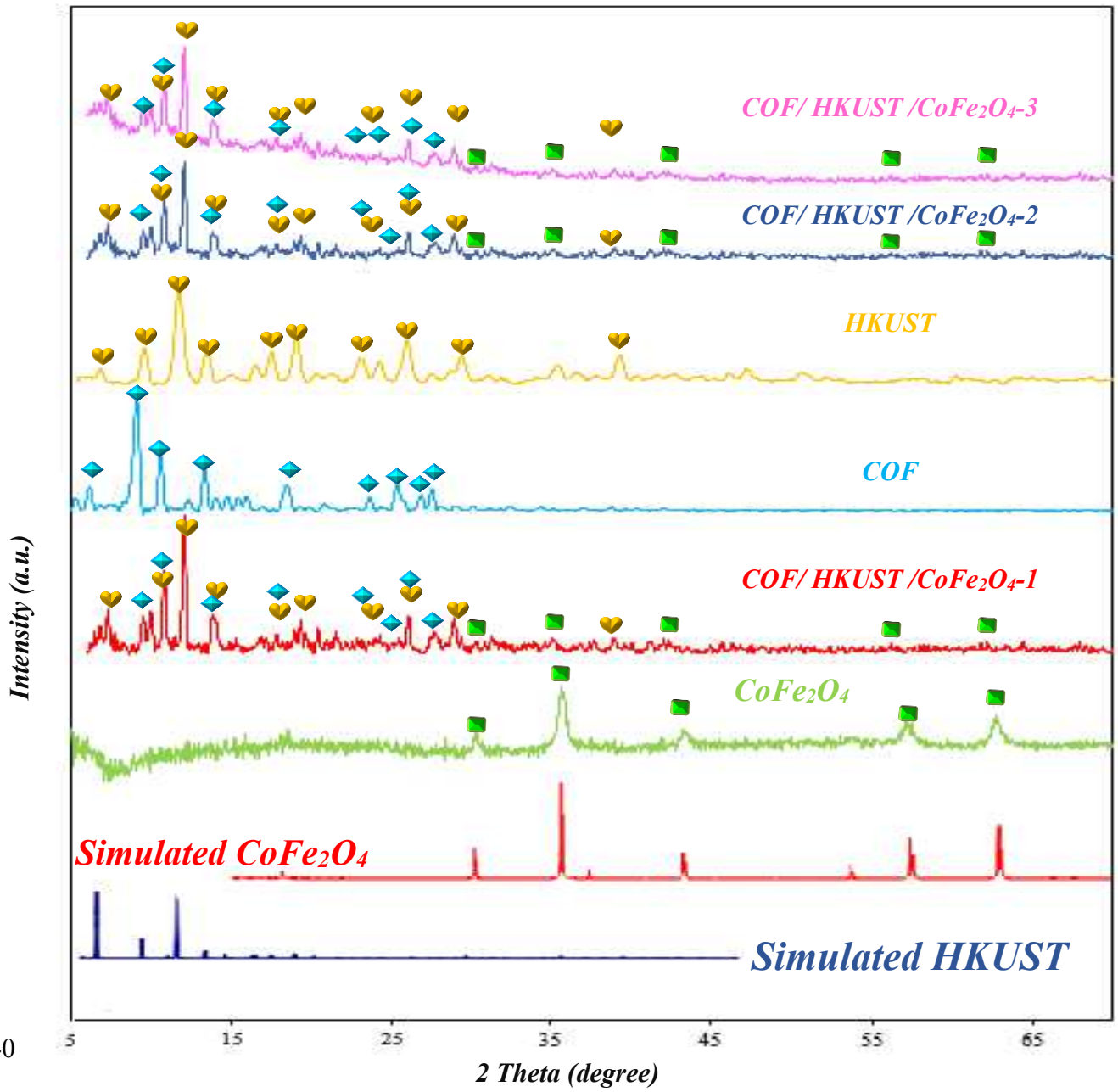
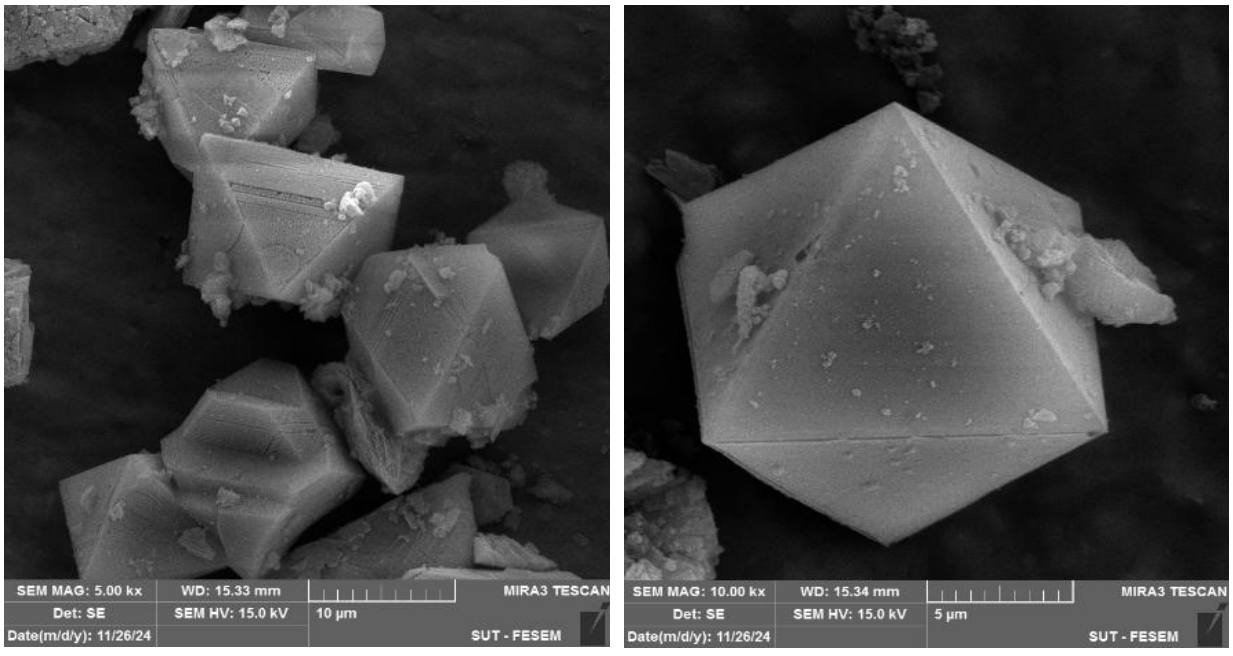


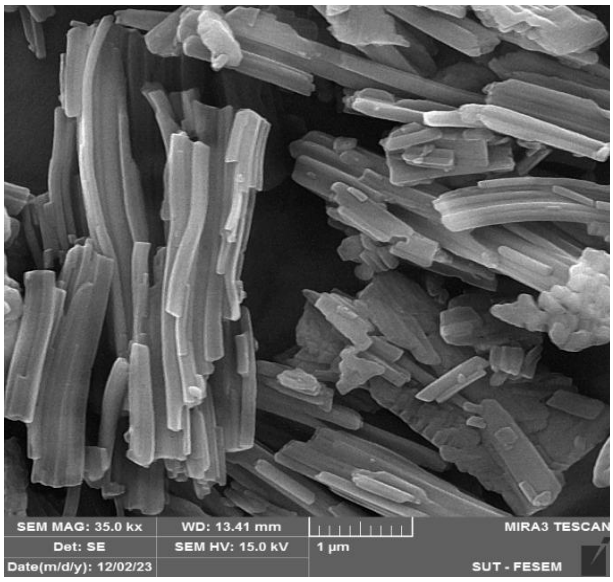
Fig. 6. The XRD patterns of the synthesized materials.

3.1.3. SEM

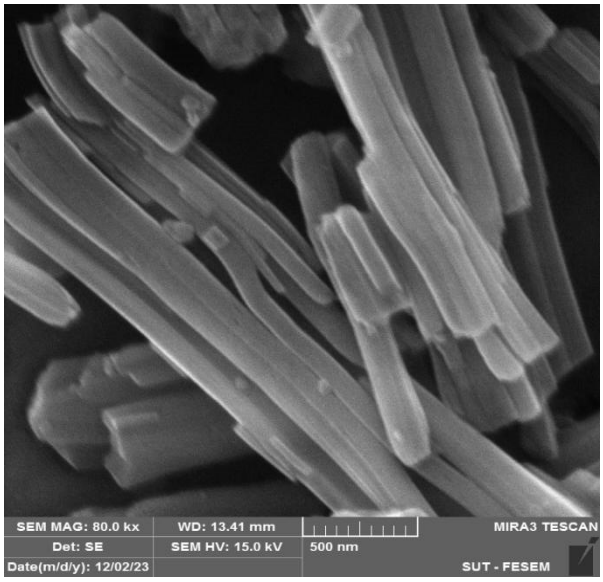
The SEM imagery elucidates the nanoscale dimensions and morphology of HKUST crystals, which are distinguished by their well-defined, discrete particle formation. These particles manifest as octahedral crystals exhibiting smooth surfaces, thereby attesting to their elevated crystallinity, as corroborated by the accompanying XRD patterns (Fig. 7a, b) [39]. The covalent organic framework with a tubular morphology features polyamide chains that were formed from distinct non-amorphous sheets. The strong hydrogen bonds between amide groups generate a three-dimensional porous network (Fig. 7c, d) [26]. Cobalt ferrite nanoparticles exhibit a relatively uniform spherical shape and identical size distribution (Fig. 7e, f) [41,42]. In the COF/HKUST/ $CoFe_2O_4$ composite images (Fig. 7g-j), the diamond-like structure of HKUST and the tubular structure of COF are easily visible with good clarity. With a little care, the magnetic cobalt ferrite particles can also be discerned. For clarity, arrows indicate the different components of the composite in the images.



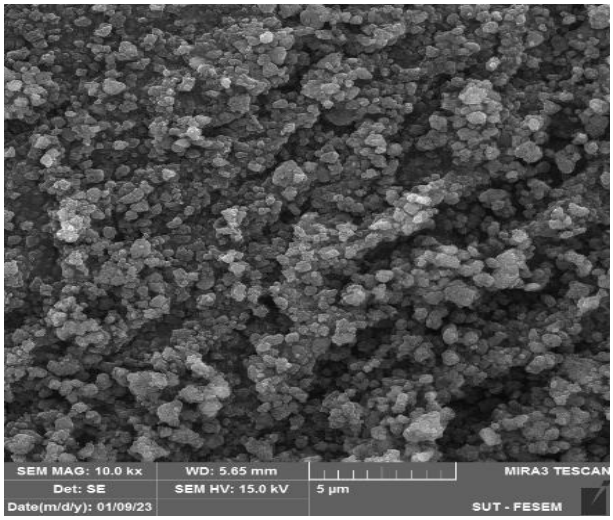
(a) (b)


SEM MAG: 35.0 kx
WD: 13.41 mm
MIRA3 TESCAN
Det: SE
SEM HV: 15.0 kV
1 µm
Date(m/d/y): 12/02/23
SUT - FESEM

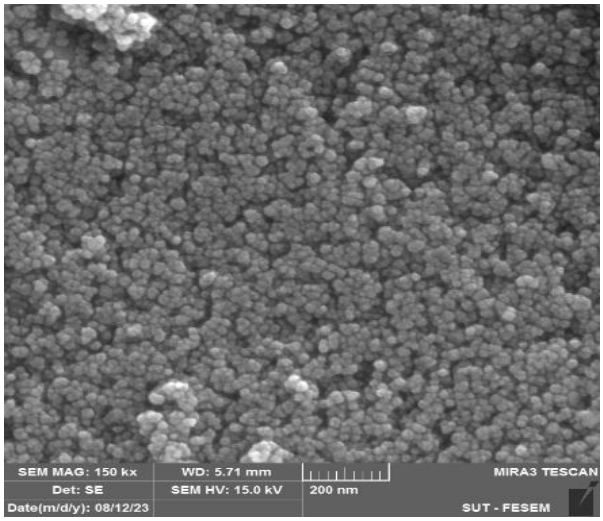
(c)


SEM MAG: 80.0 kx
WD: 13.41 mm
MIRA3 TESCAN
Det: SE
SEM HV: 15.0 kV
500 nm
Date(m/d/y): 12/02/23
SUT - FESEM

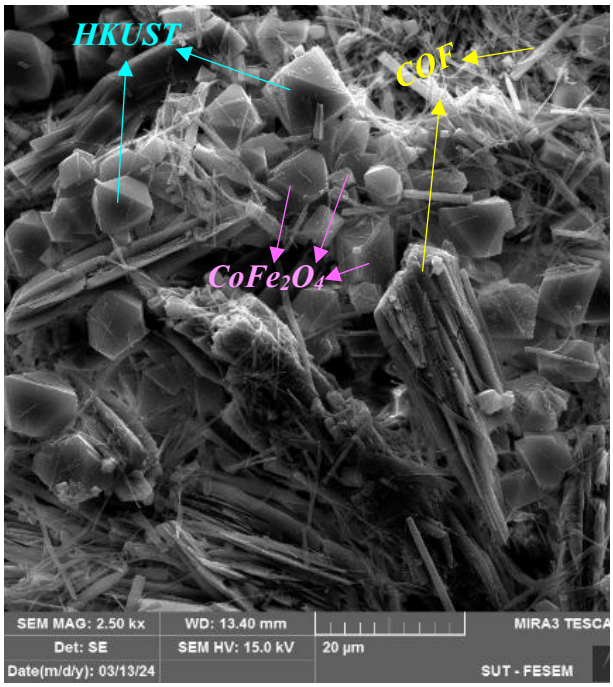
(d)


SEM MAG: 10.0 kx
WD: 5.65 mm
MIRA3 TESCAN
Det: SE
SEM HV: 15.0 kV
5 µm
Date(m/d/y): 01/09/23
SUT - FESEM

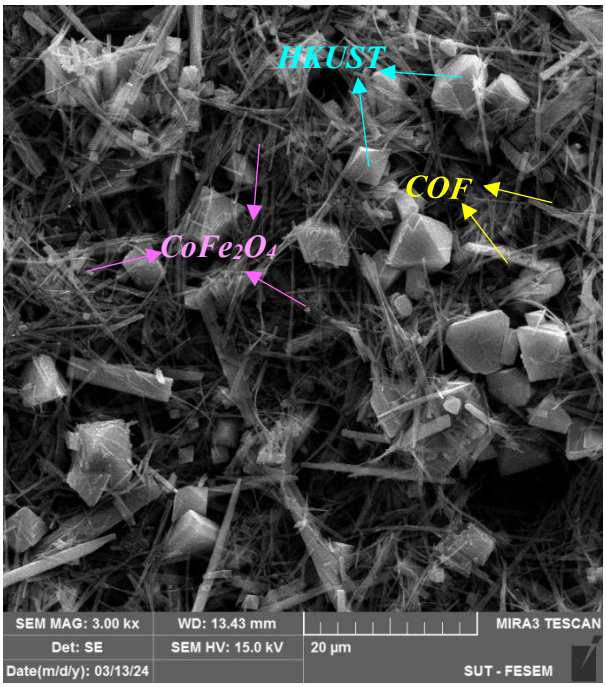
(e)


SEM MAG: 150 kx
WD: 5.71 mm
MIRA3 TESCAN
Det: SE
SEM HV: 15.0 kV
200 nm
Date(m/d/y): 08/12/23
SUT - FESEM

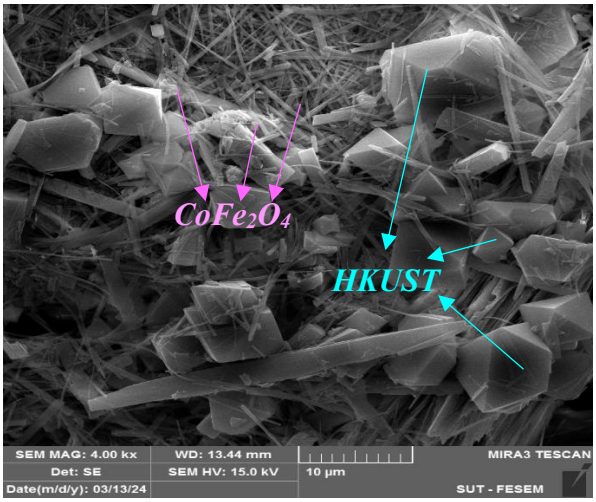
(f)



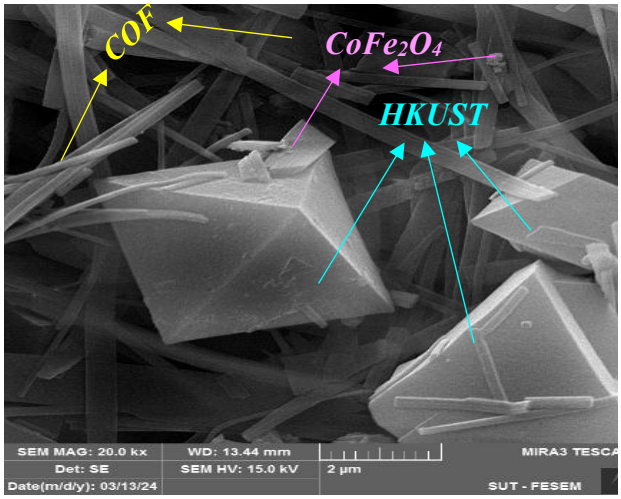
(g)



(h)



(i)



(j)

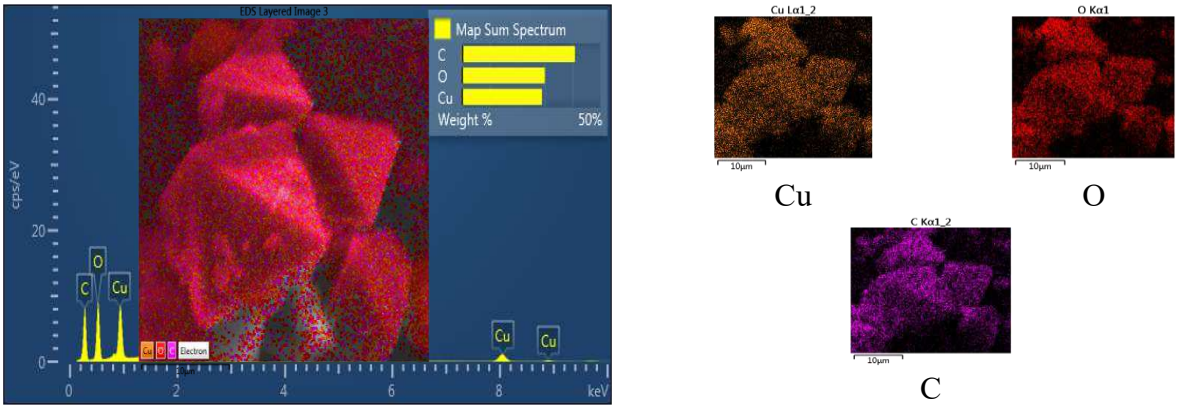
256 Fig. 7. SEM images of HKUST (a, b), COF (c, d), $CoFe_2O_4$ (e, f),COF/HKUST/ $CoFe_2O_4$ -1(g),
257 COF/HKUST/ $CoFe_2O_4$ -2 (h), COF/HKUST/ $CoFe_2O_4$ -3(i), COF/HKUST/ $CoFe_2O_4$ (j)
258
259

3.1.4. MAP and EDX

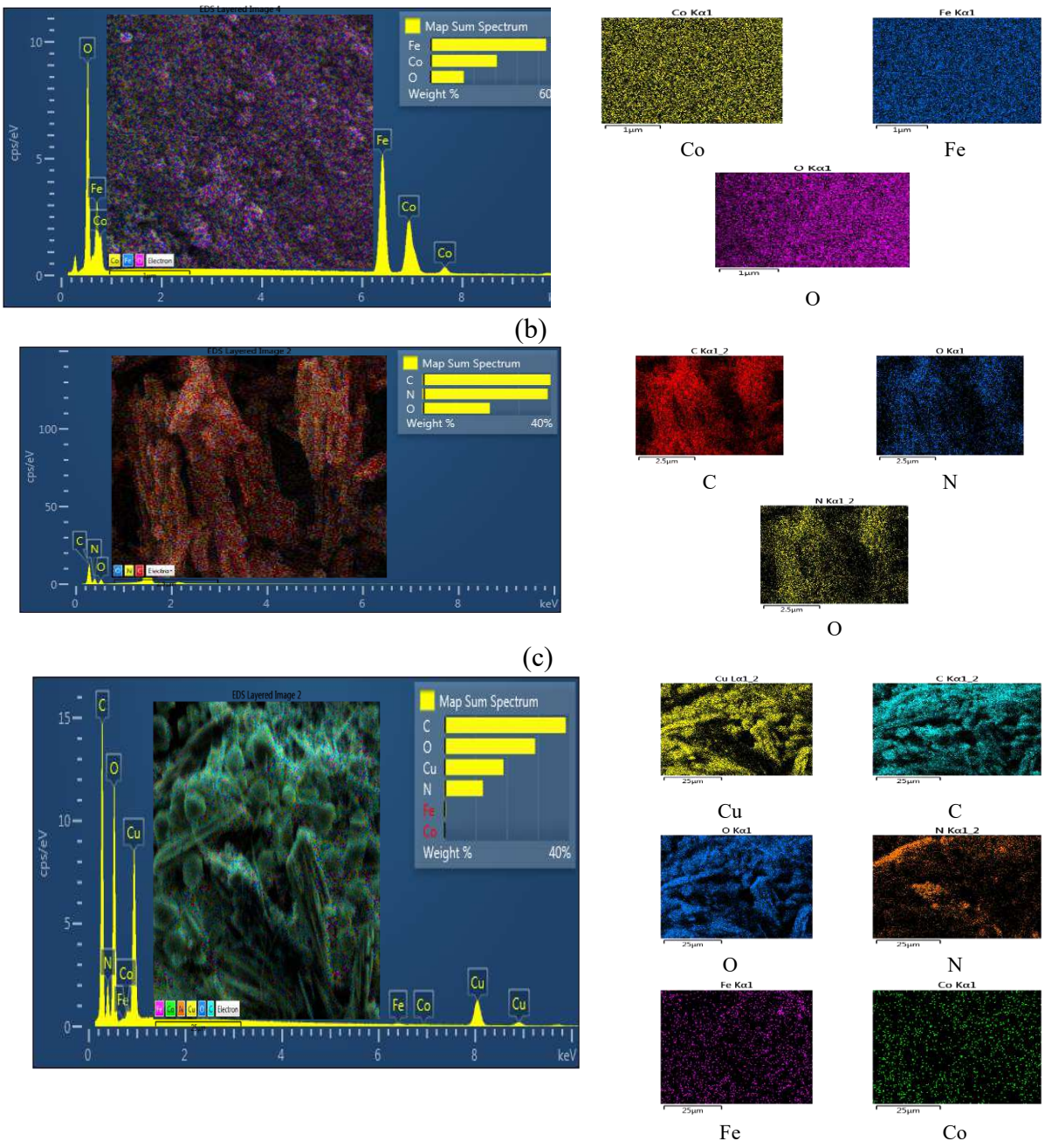
The elemental composition of materials was assessed (Fig. 8). In COF, the elements carbon, nitrogen, and oxygen were detected, whereas HKUST revealed the presence of copper, carbon, and oxygen. In the case of cobalt ferrite, the constituent elements identified included oxygen, cobalt, and iron. As anticipated, in the COF/HKUST/$CoFe_2O_4$ composite, the presence of carbon and nitrogen, and oxygen associated with the COF, alongside oxygen, copper, and carbon pertaining to HKUST, as well as cobalt, iron, and oxygen linked to cobalt ferrite, can be identified. This observation serves as a corroboration of the composite synthesis. The percentage of elements present in each material, is shown in Table 2.

Table 2. Elemental content of synthesized materials

Name	**C**	**O**	**Fe**	**N**	**Co**	**Cu**	**Total**
HKUST	40.93	30.08	-	-	-	28.99	100
COF	39.93	21.03	-	39.04	-	-	100
$CoFe_2O_4$	-	15.47	53.69	-	30.85	-	100
COF/HKUST/ $CoFe_2O_4$	38.95	29.13	0.46	12.34	0.19	18.94	100



(a)



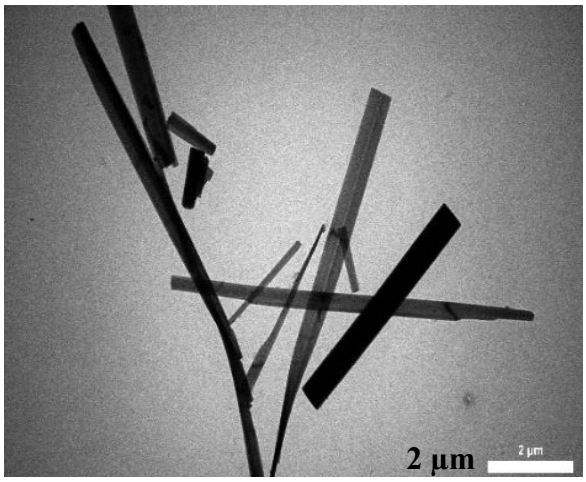
273 Fig. 8. EDX and MAP of materials (a) HKUST, (b) $CoFe_2O_4$, (c) COF, and (d)

274 COF/HKUST/$CuFe_2O_4$

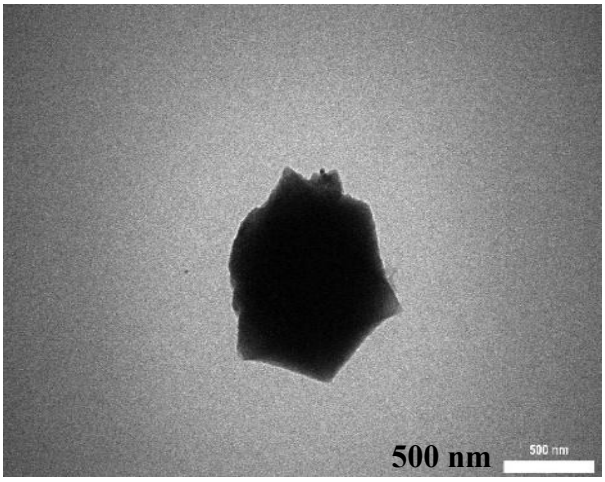
275

3.1.5. TEM

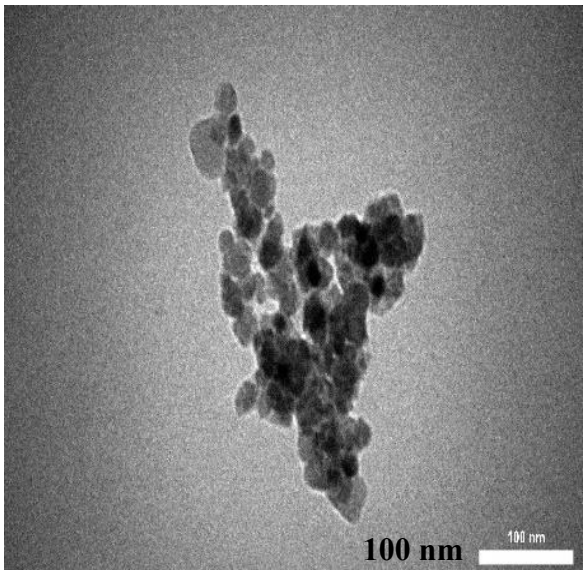
Fig. 9 displays the TEM image of the COF/HKUST/CoFeO4 composite and its constituent materials, clearly are identifiable the magnetic cobalt ferrite nanoparticles[41], HKUST-1[43] and COF crystals. The ternary magnetic composite distinctly shows the integration of all three materials, in ternary COF/HKUST/$CuFe_2O_4$ composite[44].



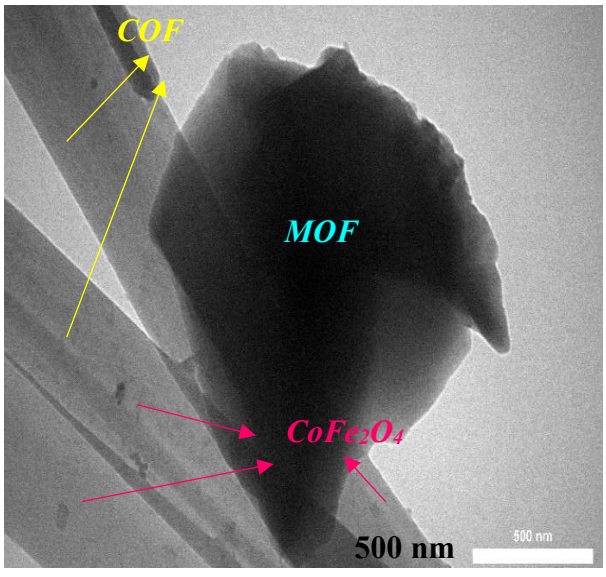
(a)



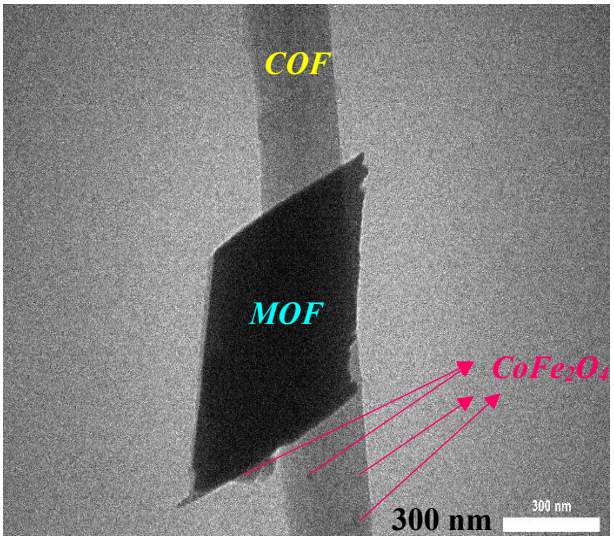
(b)



(c)



(d)

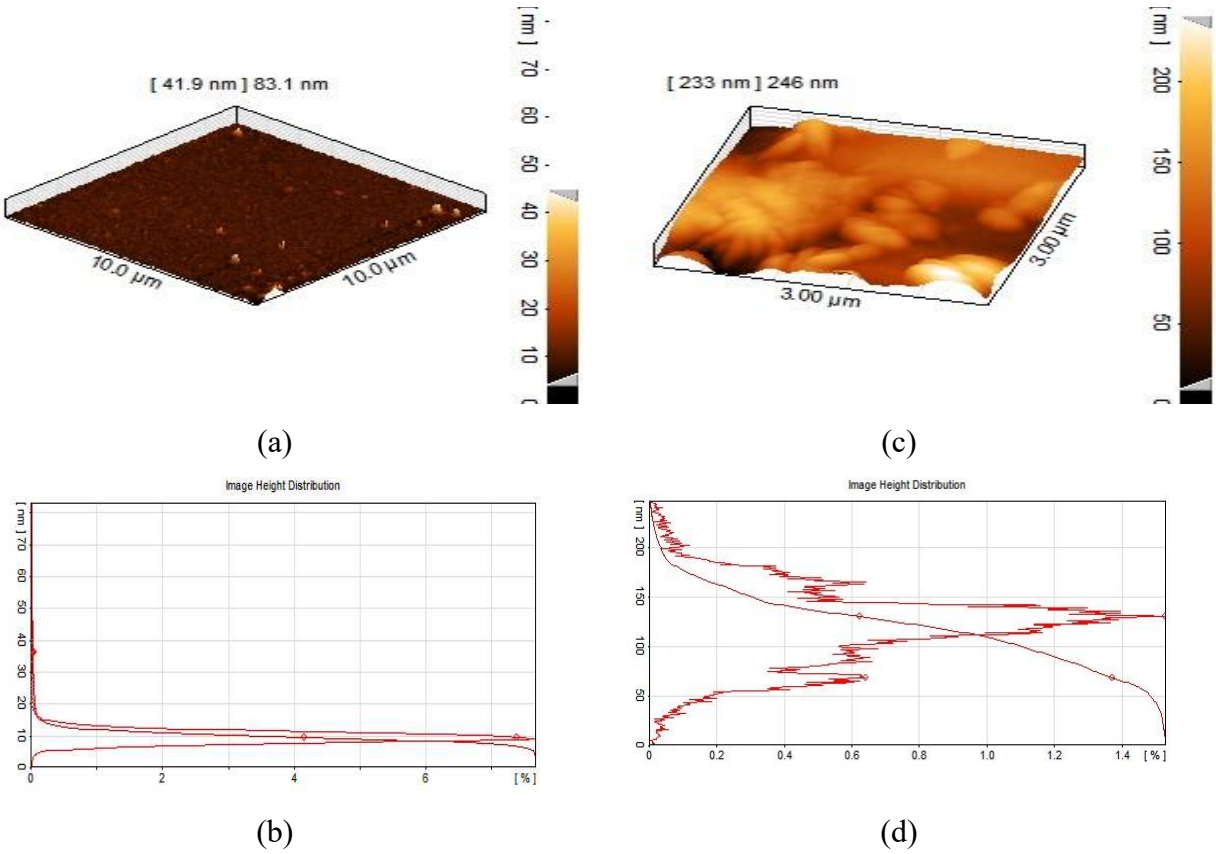


(e)

Fig. 9. TEM image of materials (a) HKUST, (b) $CoFe_2O_4$, (c) COF, and (d, e) COF/HKUST/ $CoFe_2O_4$ composite

3.1.9. AFM

To assess the surface roughness of the covalent organic framework (COF) before and after synthesizing the magnetic composite, a 3D topographic map was analyzed (Fig. 10). The increase in composite surface roughness from 83 to 246 nm, along with the varied size and shape of particles, confirms the successful incorporation of the metal-organic framework and nanoparticles into the COF. The particle distribution reveals three distinct sizes corresponding to cobalt ferrite, the metal-organic framework, and the covalent organic framework, indicating the presence of all three materials in the composite [45].



292 Fig. 10. AFM analysis of materials (a and b) COF and (c and d) COF/HKUST/$CoFe_2O_4$
293 composite

294

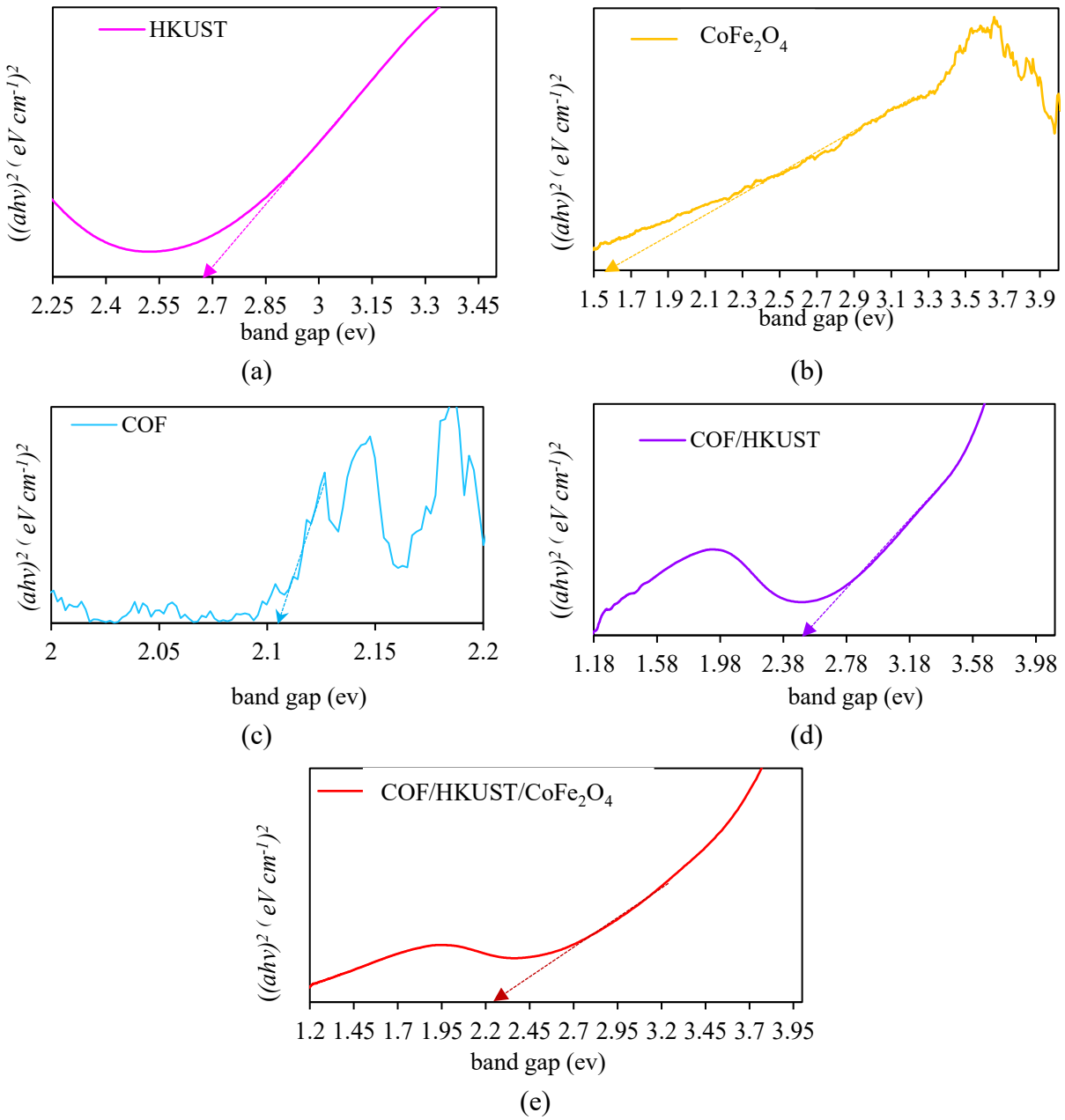
295 ***3.1.7. DRS***

296 DRS allows to assess a material's photocatalytic performance and calculating band gap, offering
297 insights into the structure of photocatalysts that can by using them enhance their efficiency in
298 pollutant degradation. In fact, deep understanding of the electronically transitions of catalysts not
299 only aids in identifying potential photocatalysts but also in fine-tuning their composition and
300 morphology for optimal performance. In the Tauc method, the band gap energy is found by
301 extrapolating the absorption edge to the x-axis. The advancement of composite photocatalysts that
302 integrate diverse porous materials with varying band gaps can take leverage synergistic effects,
303 increasing the light absorption range, and optimizing the separation of charge carriers. The band

304 gap is 2.65, 1.6, 2.12, 2.48 and 2.35 eV for HKUST, $CoFe_2O_4$, COF, COF/HKUST/$CoFe_2O_4$, and

305 COF/HKUST/$CoFe_2O_4$ composites (Fig. 11).

306



307 Fig. 11. The band gap energy of the (a) HKUST, (b) $CoFe_2O_4$, (c), COF (d) COF/HKUST binary
308 composite, (e) COF/HKUST/$CoFe_2O_4$ ternary composite

3.1.8. VSM

Fig. 12 illustrates the magnetic properties and hysteresis loops of $CoFe_2O_4$ nanoparticles, a metal-organic framework (MOF), and their composite COF/HKUST/ $CoFe_2O_4$, as assessed via VSM. The VSM data confirms the successful fabrication of a magnetic composite, demonstrating the integration of the magnetic $CoFe_2O_4$ phase with HKUST and COF while preserving its magnetic characteristics. The ternary composite exhibits a saturation magnetization of approximately 6 emu /g, rendering it suitable for magnetic separation and reusability. This suggests a composite structure wherein $CoFe_2O_4$ nanoparticles are either encapsulated within the MOF/COF matrix or deposited on the surface of the larger HKUST/COF particles. Hysteresis loop analysis revealed that the pristine cobalt ferrite nanoparticles exhibit characteristic ferrimagnetic behavior, with a high saturation magnetization of 30 emu /g and a coercivity of 350 Oe, confirming their magnetic hardness. Upon formation of the ternary composite, a significant reduction in saturation magnetization to 6.0 emu/g was observed, accompanied by an increase in coercivity to 450 Oe. The substantial decrease in magnetization results from the diamagnetic contribution of the HKUST and COF components, providing compelling evidence of successful composite formation. The retained magnetic hysteresis in the composite ensures its separability via external magnetic fields. Notably, the pure HKUST displayed a weak magnetic signal (magnetization = 1.42 emu/g, coercivity = 100 Oe), potentially originating from paramagnetic metal clusters[41,46].

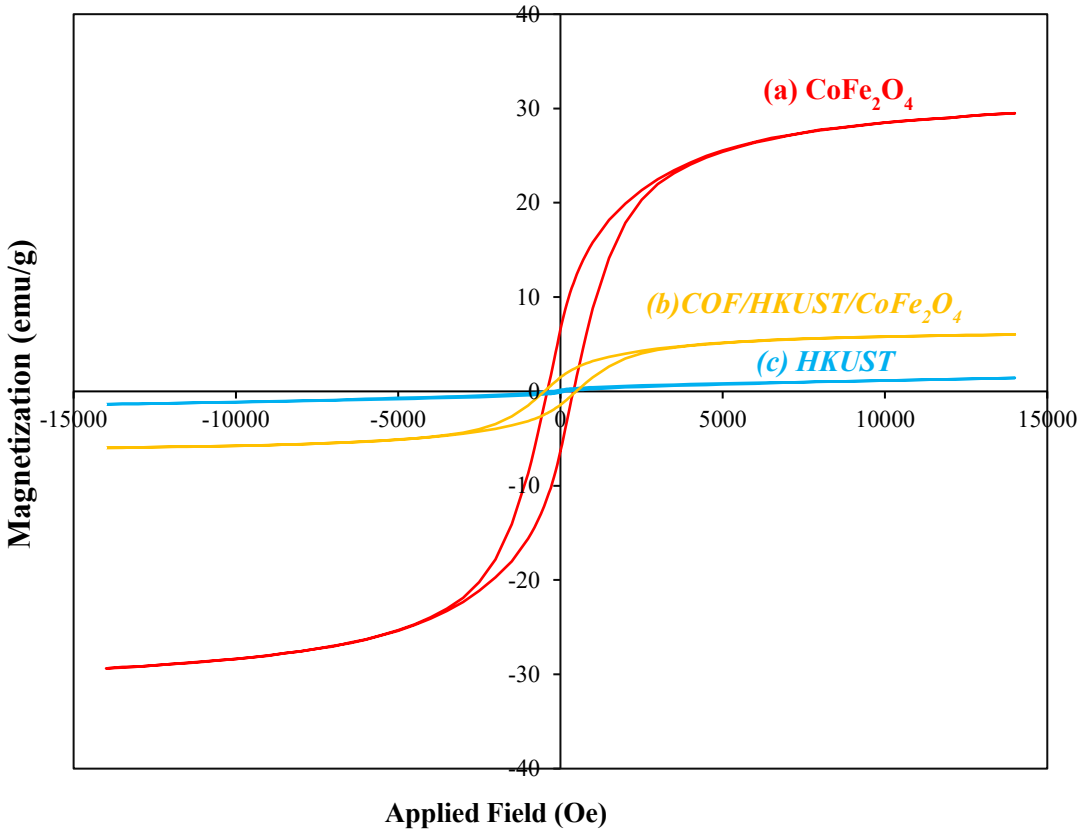


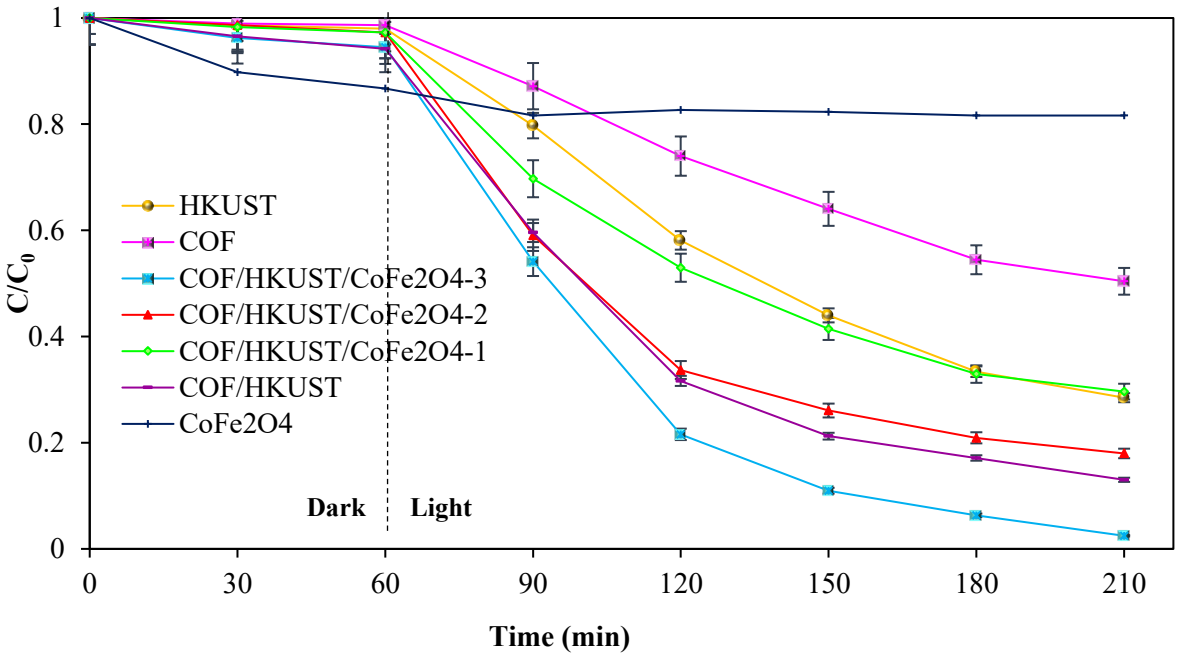
Fig. 12. Comparing magnetic properties of $CoFe_2O_4$ (a), COF/HKUST/$CoFe_2O_4$ composite (b), HKUST(c)

3.2. Contaminant removal

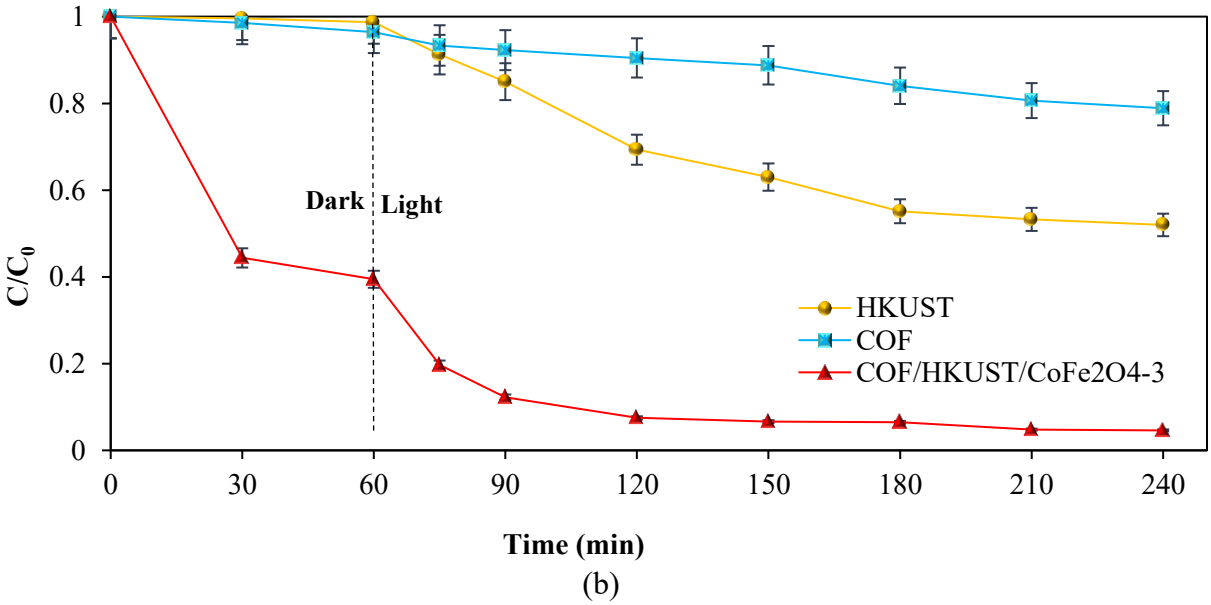
3.2.1. *COF, HKUST, and COF/HKUST/$CoFe_2O_4$* degradation ability

A comparative evaluation assessed the performance of the composites and their components. In Fig. 13, the COF/HKUST/$CoFe_2O_4$ ternary composite-3 exhibited the best performance, removing 97% of the MB, compared to 82% and 76% for composites 2 and 1, respectively. The binary COF/HKUST composite-3 (without cobalt ferrite) ranked second with 89% removal, then, HKUST (73%) and COF (49%). The better performance of the ternary composite, compared to its binary counterpart, arises from the synergistic interaction of its components. The COF/HKUST heterojunction functions as the primary photocatalytic center, while the integrated $CoFe_2O_4$

nanoparticles promote enhanced charge separation by acting as electron acceptors, thereby mitigating electron-hole recombination.



(a)

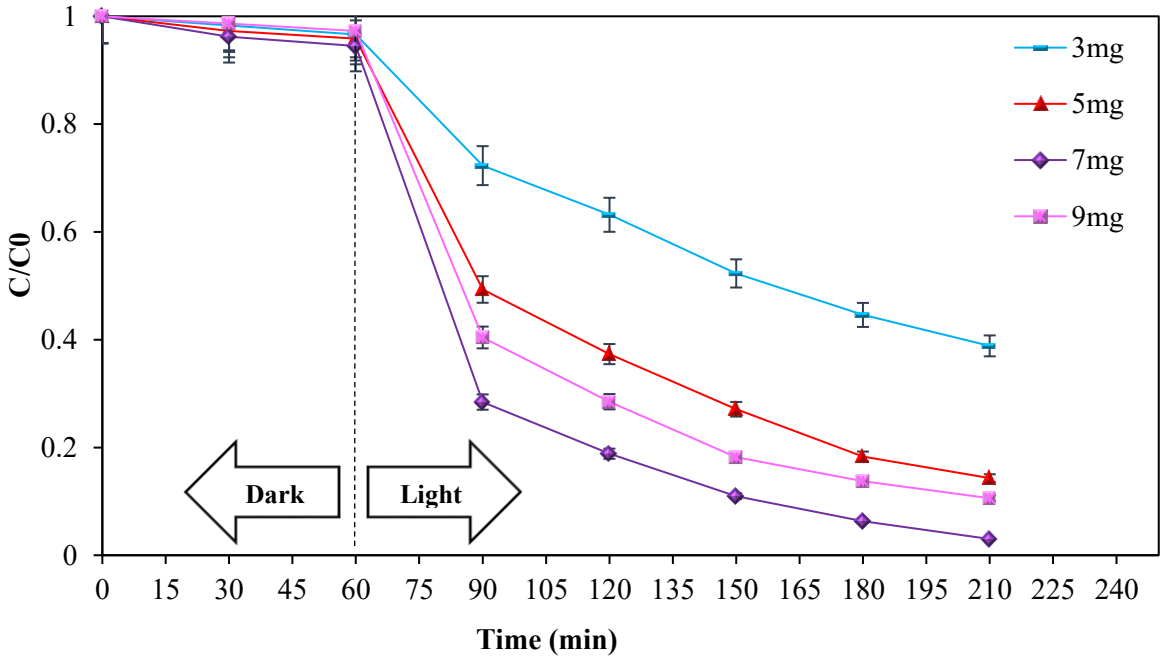


(b)

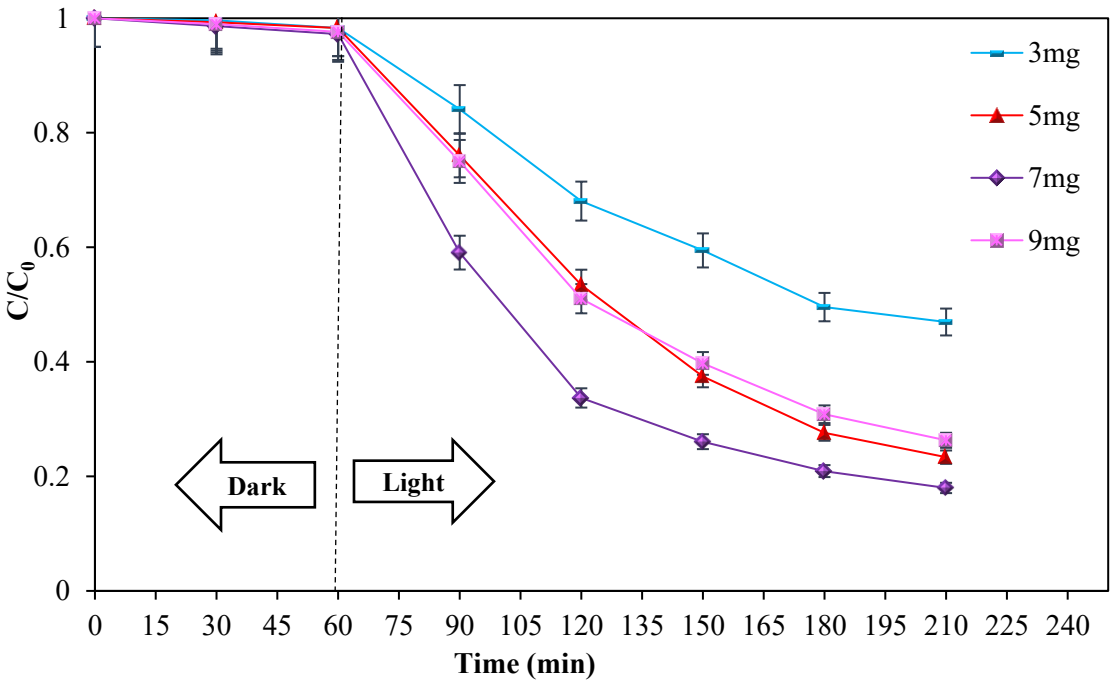
Fig. 13. Comparison of COF, HKUST, $CoFe_2O_4$, binary COF/HKUST and ternary COF/HKUST/$CoFe_2O_4$ composites considering component content, in degradation of MB (20 mg/L at natural pH with 20µL H_2O_2) (a), and DOX (90 mg/L at natural pH with 20µL H_2O_2) (b)

3.2.2. Catalyst dosage

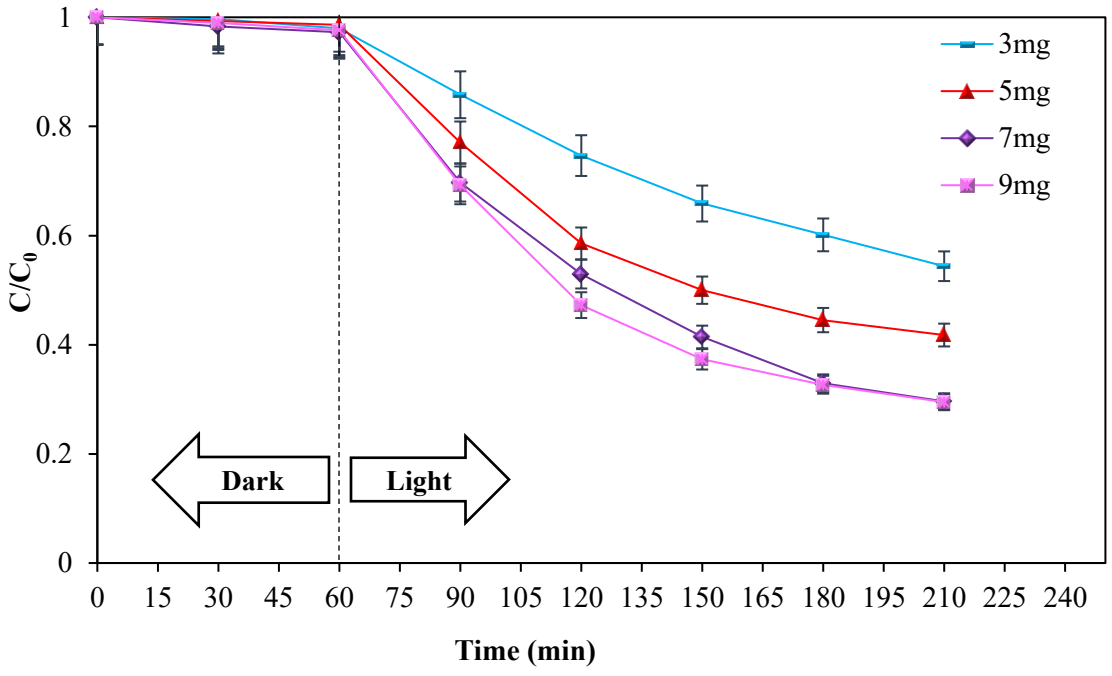
As the catalyst concentration increases, the light-exposed catalytic surface area expands, resulting in a significant rise in the production of electron-hole pairs and active radicals. This enhancement improves both pollutant degradation and catalyst efficiency (Fig. 14). In the optimized ternary composite COF/HKUST/$CoFe_2O_4$-3 a catalyst dose of 3 mg yielded a methylene blue degradation rate of 61%. Increasing the dose to 7 mg enhanced the degradation to 97% in a 20 mg/L MB solution at normal pH. However, a further increase to 9 mg resulted in a decrease in degradation, reducing MB degradation to 89%. A similar MB degradation trend is observed for the other ternary composites. Increased catalyst dosage may cause accumulation, reducing the surface area available for contaminant interaction and light exposure, thereby disrupting the degradation process. Additionally, heightened turbidity in the photocatalytic system decreases incoming light penetration[47,48]. Interestingly, the degradation of the pharmaceutical contaminant doxycycline improved with higher catalyst dosages; specifically, as the dosage increased from 4 to 10 mg, the degradation of a 90 mg/L doxycycline solution raised from 67% to 95%[49].


C/C0
Time (min)
3mg
5mg
7mg
9mg
Dark
Light

(a)


C/C0
Time (min)
3mg
5mg
7mg
9mg
Dark
Light

(b)



(c)

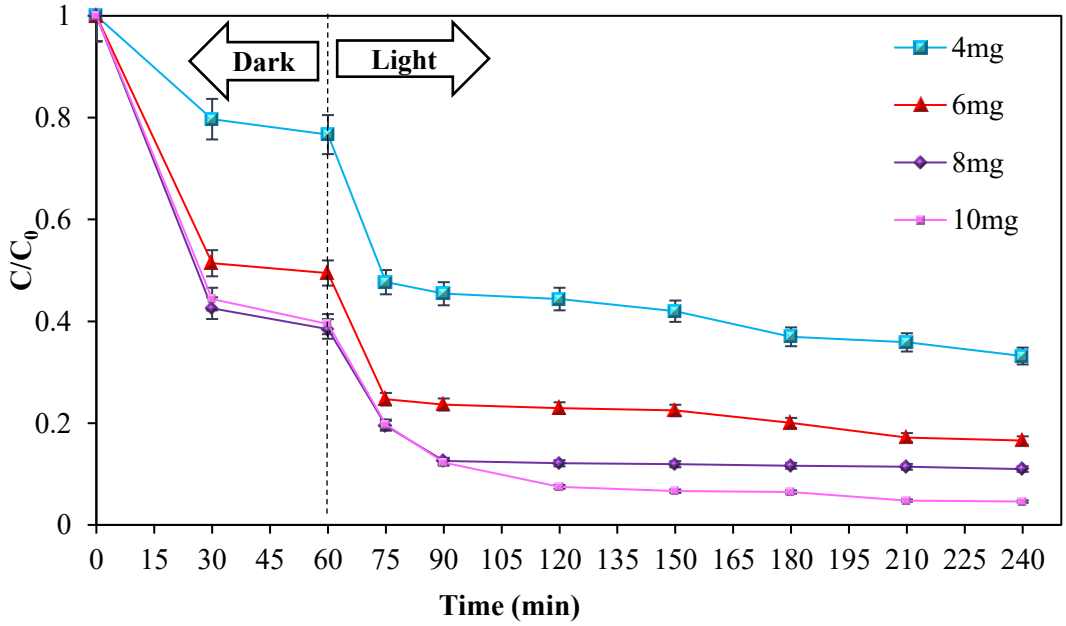
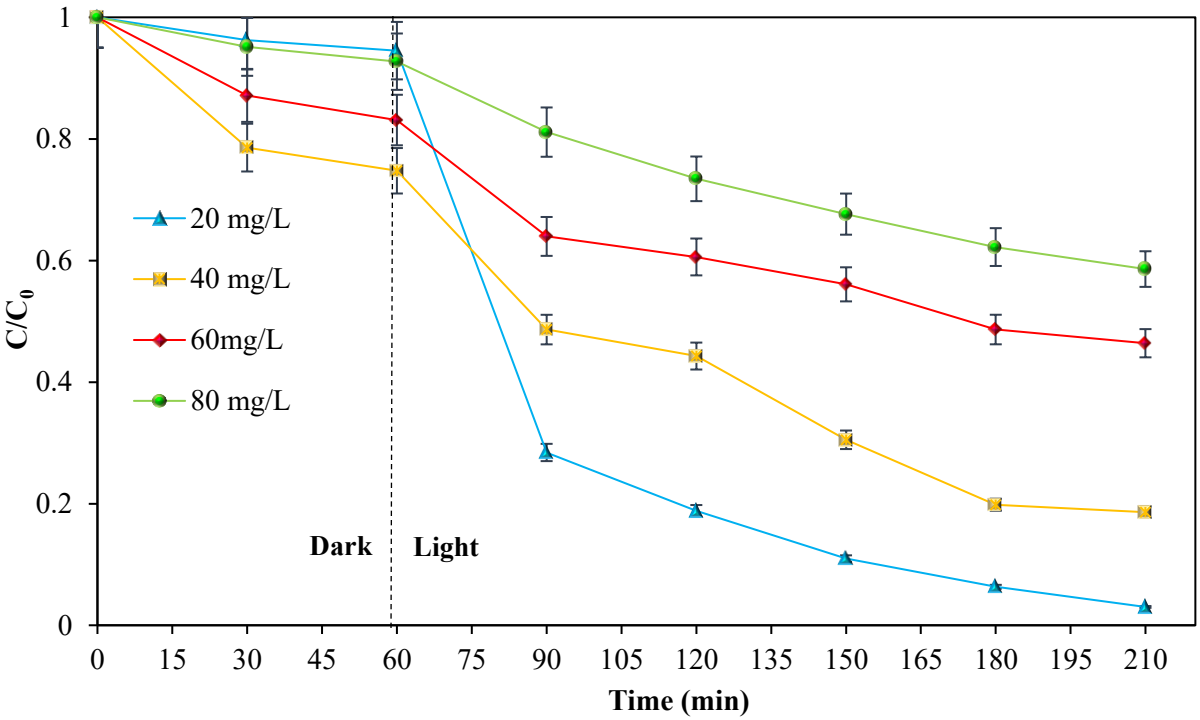


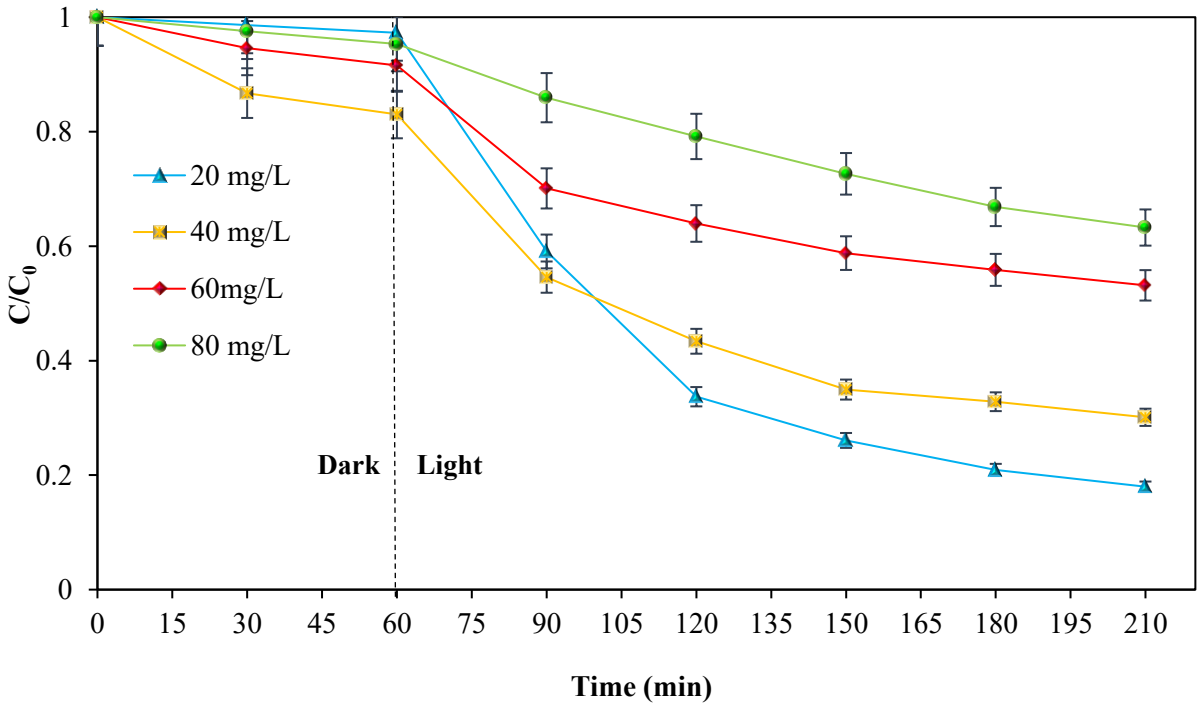
Fig. 14. The catalyst dosage effect on pollutant degradation ((a) COF/HKUST/$CoFe_2O_4$-3, (b)COF/HKUST/$CoFe_2O_4$-2, (c) COF/HKUST/$CoFe_2O_4$-1 for the MB (20 mg/L at natural pH with 20µL H_2O_2), and (d) COF/HKUST/$CoFe_2O_4$-3 for the DOX (90 mg/L at natural pH with 20µL H_2O_2)).

3.2.3. Contaminant concentration

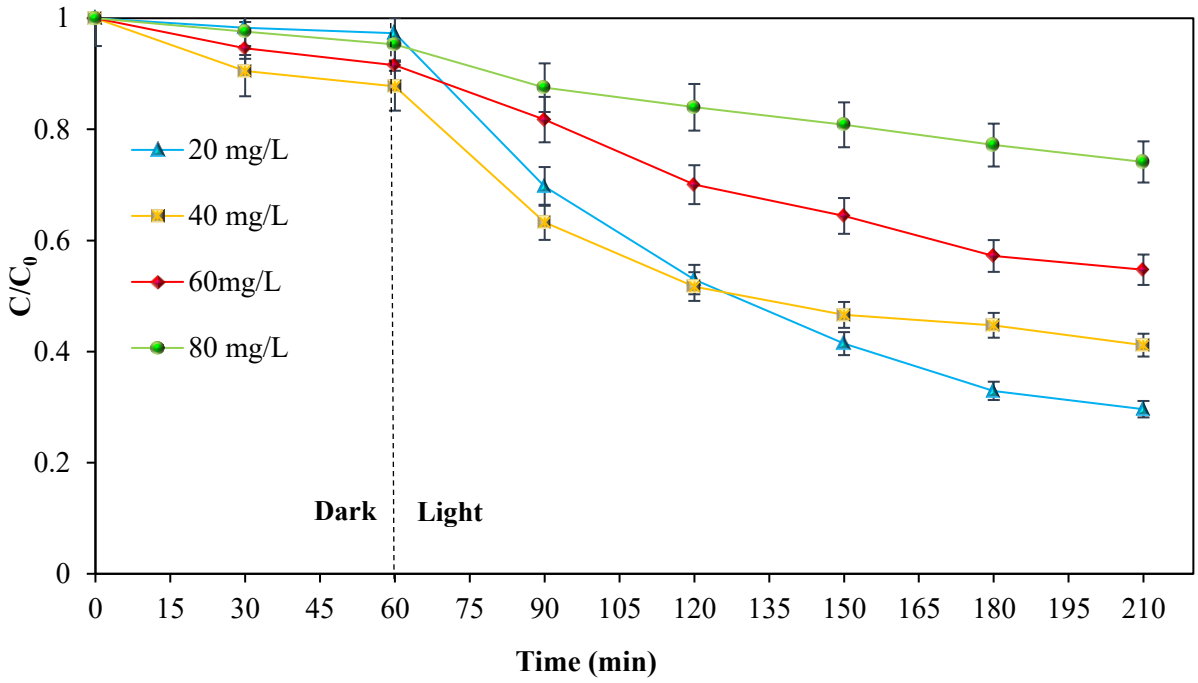
Following optimization of the dosage of magnetic ternary composite, the impact of initial pollutant concentration on degradation rate was investigated (Fig. 15). Solutions of doxycycline (70, 90, 120, and 150 mg/L) and methylene blue (20, 40, 60, and 80 mg/L) were prepared at their natural pH. The catalyst was introduced to 100 mL of each solution at a concentration of 10 mg for doxycycline and 7 mg for methylene blue. Following the establishment of adsorption-desorption equilibrium in the dark, the solutions were exposed to visible light, with the addition of 20 µL of H_2O_2. The results indicated that decreased pollutant concentrations correlated with increased light penetration, enhanced electron-hole pair generation, and elevated formation of reactive radicals. Consequently, the pollutant degradation rate and photocatalytic performance were improved. Fig. 15 revealed minimal difference in removal performance at 70 and 90 mg/L of DOX, but the optimal at 90 mg/L, 95.4%, is significantly better than at 150 mg/L, 45.5%. At a MB concentration of 20 mg/L, ternary COF/HKUST/$CoFe_2O_4$ composite-3 exhibited the highest degradation rate (97%), followed by ternary COF/HKUST/$CoFe_2O_4$ composite-2 (82%) and ternary COF/HKUST/$CoFe_2O_4$ composite-1 (70.4%). When the concentration was increased to 80 mg/L, the degradation rates for all composites decreased, with ternary composite-3 showing 41% degradation, ternary composite-2 showing 36.7% degradation, and ternary composite-1 showing 25.8% degradation [50].


1
0.8
0.6
0.4
0.2
0
C/C0
20 mg/L
40 mg/L
60mg/L
80 mg/L
Dark
Light
0
15
30
45
60
75
90
105
120
135
150
165
180
195
210
Time (min)

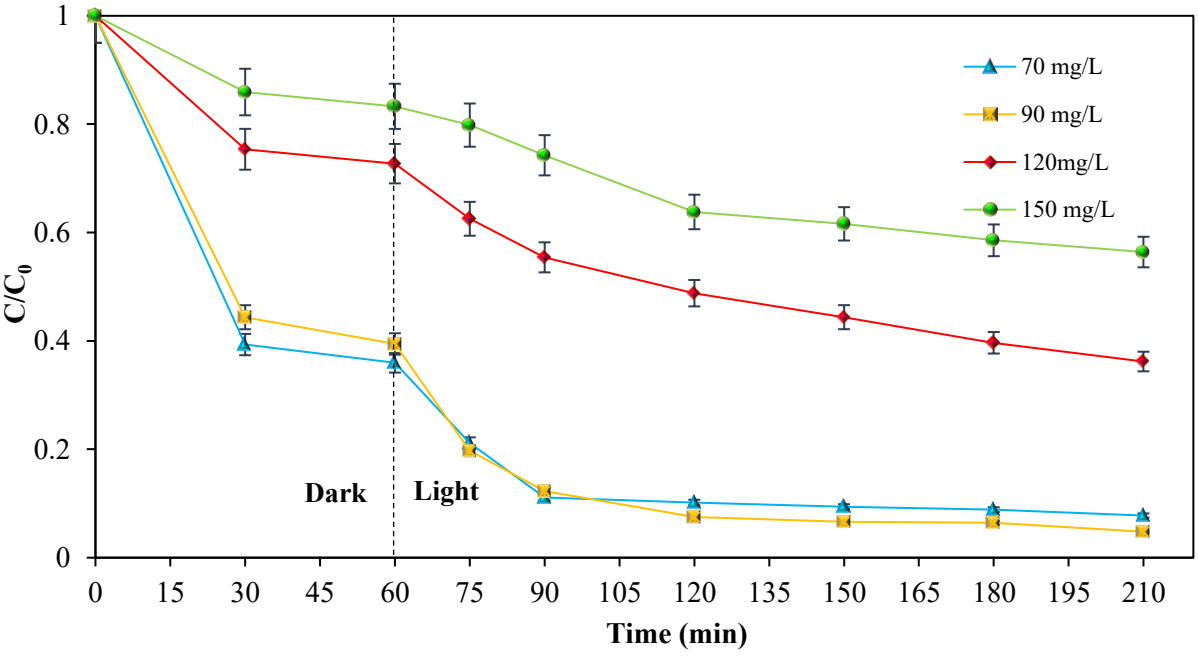
(a)


1
0.8
0.6
0.4
0.2
0
C/C0
20 mg/L
40 mg/L
60mg/L
80 mg/L
Dark
Light
0
15
30
45
60
75
90
105
120
135
150
165
180
195
210
Time (min)

(b)



(c)



(d)

Fig. 15. The impact of initial concentrations on pollutant degradation using catalysts ((a) COF/HKUST/$CoFe_2O_4$-3, (b)COF/HKUST/$CoFe_2O_4$-2, (c) COF/HKUST/$CoFe_2O_4$-1 for the MB (0.07 mg/L photocatalyst at natural pH with 20µL H_2O_2), and (d) COF/HKUST/$CoFe_2O_4$-3 for the DOX (0.1 mg/L at natural pH with 20µL H_2O_2))

3.2.5. Degradation kinetics

The degradation of pollutants by COF/HKUST/$CoFe_2O_4$ was evaluated using three types of kinetics. Data indicate that in the DOX degradation followed the second-order and methylene blue degradation obeyed the first-order kinetics, both demonstrating better correlation coefficients (Table 3 and Figs. 16-18) [51].

Table 3. The DOX and MB degradation kinetics using COF/HKUST/$CoFe_2O_4$

Photocatalyst	***Pollutant***	***Concentration (mg/L)***	***Zero-order*** $C - C_0 = -k_0t$		***First-order*** $Ln\ (C/C0) = k_1t$		***Second-order*** $(1/C) - (1/C_0) = k_2t$	
			k_0 (mg/min L)	R^2	k_1 (1/min)	R^2	k_2 (L/mg min)	R^2
COF/HKUST/$CoFe_2O_4$-1	MB	20	0.070	0.9214	0.0055	0.9133	0.0005	0.8649
		40	0.1284	0.9193	0.0046	0.9454	0.0002	0.9504
		60	0.1355	0.9757	0.0029	0.9657	6E-05	0.9429
		80	0.1005	0.9808	0.0014	0.9798	2E-05	2E-05
COF/HKUST/$CoFe_2O_4$-2	MB	20	0.0863	0.8903	0.0081	0.9074	0.0009	0.8664
		40	0.155	0.918	0.0062	0.9554	0.0003	0.9478
		60	0.1507	0.9265	0.0033	0.9451	7E-05	0.9534
		80	0.1391	0.9662	0.0021	0.9536	3E-05	0.9338
COF/HKUST/$CoFe_2O_4$-3	MB	20	0.1067	0.8504	0.0149	0.918	0.0045	0.6342
		40	0.1759	0.9436	0.008	0.9684	0.0004	0.8561
		60	0.1736	0.9284	0.0039	0.9711	4E-05	0.9589
		80	0.164	0.9789	0.0025	0.9746	9E-05	0.9786
	DOX	70	0.3849	0.405	0.014	0.648	0.0008	0.9248
		90	0.3035	0.7424	0.0157	0.8102	0.001	0.9435
		120	0.2494	0.8573	0.0051	0.9303	8E-05	0.9921
		150	0.3401	0.8573	0.0029	0.9283	3E-05	0.9651

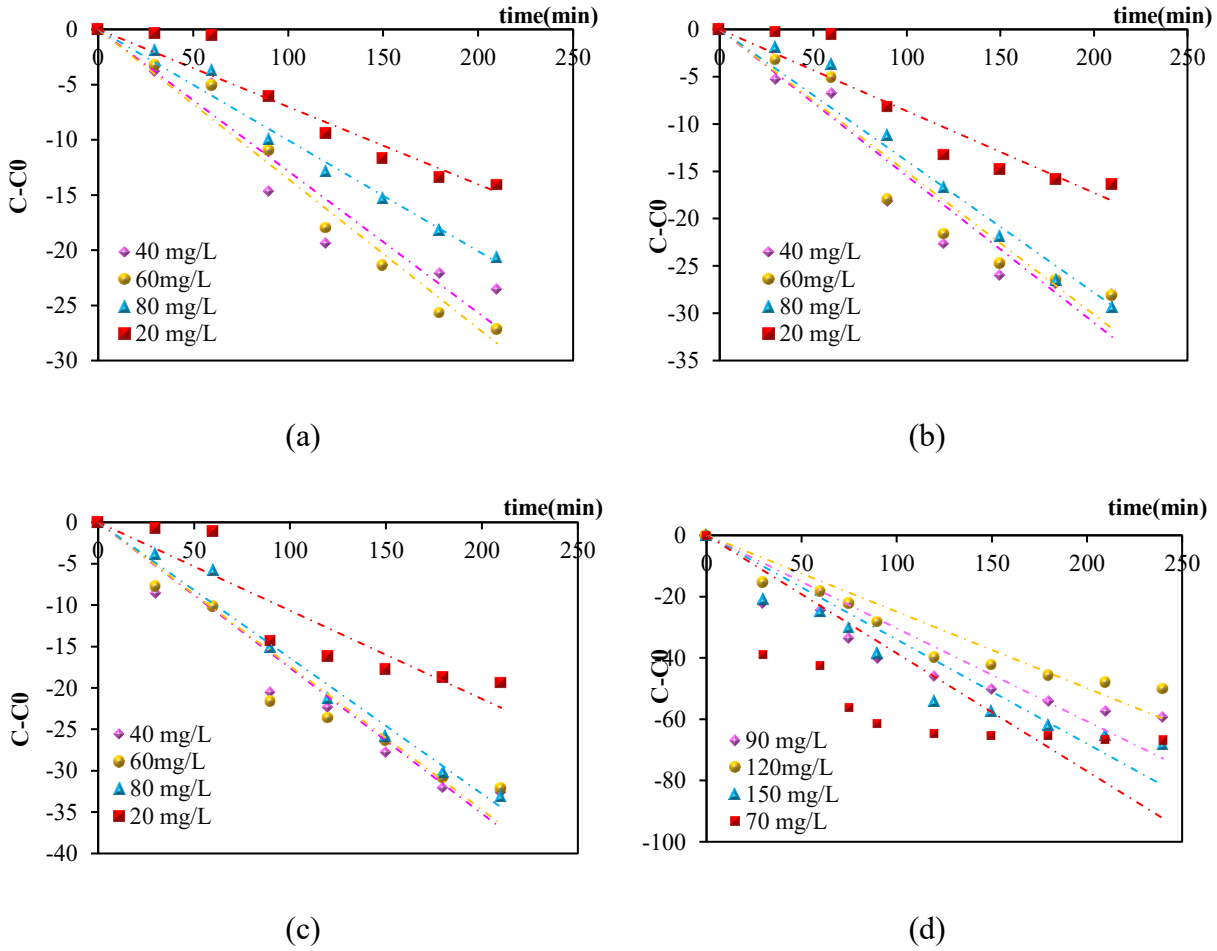


Fig. 16. Contaminant photocatalytic degradation kinetics (zero-order) using COF/HKUST/$CoFe_2O_4$-1 (a) COF/HKUST/$CoFe_2O_4$-2 (b) COF/HKUST/C $CoFe_2O_4$-3 (c) for MB, and COF/HKUST/ $CoFe_2O_4$ -3 (d) for DOX

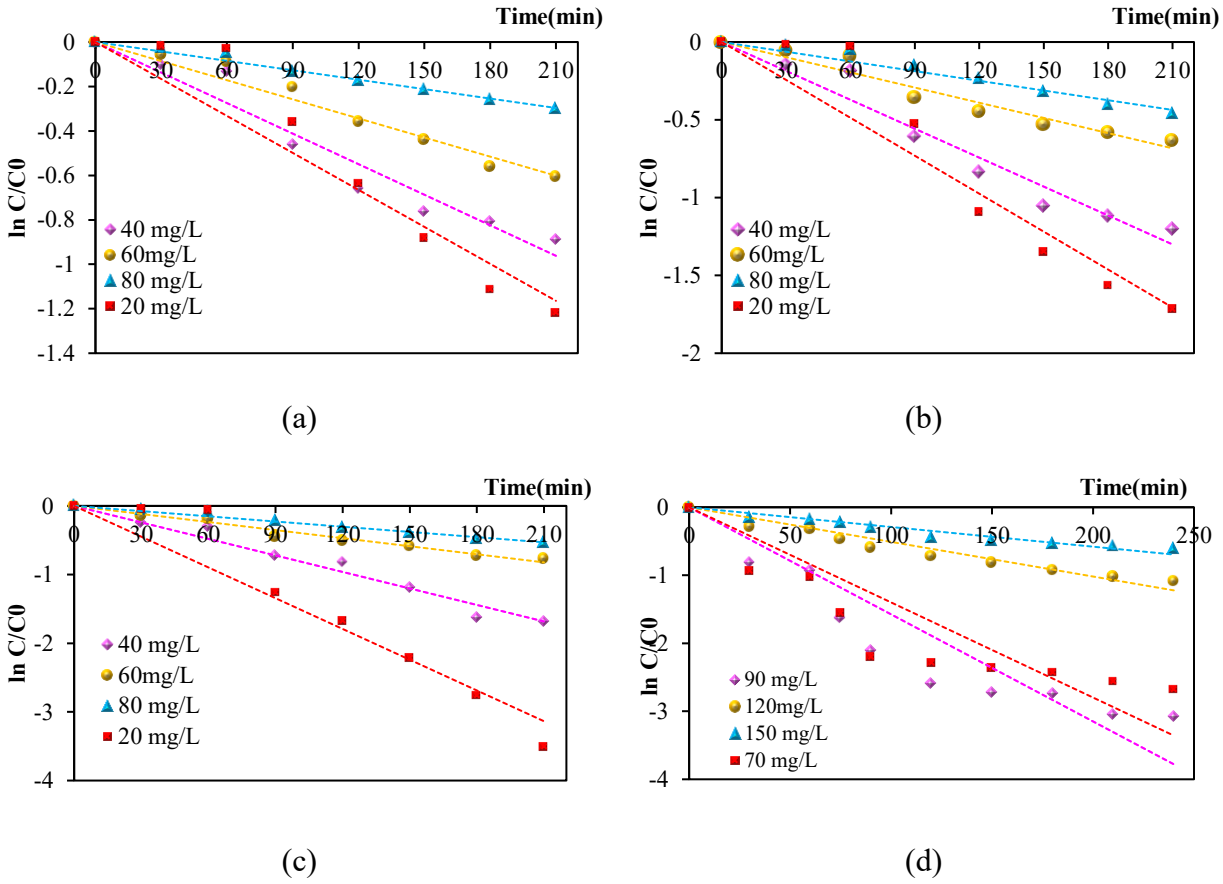


Fig. 17. Contaminant photocatalytic degradation kinetics (First-order) using COF/HKUST/$CoFe_2O_4$-1 (a) COF/HKUST/$CoFe_2O_4$-2 (b) COF/HKUST/C $CoFe_2O_4$-3 (c) for MB, and COF/HKUST/ $CoFe_2O_4$ -3 (d) for DOX

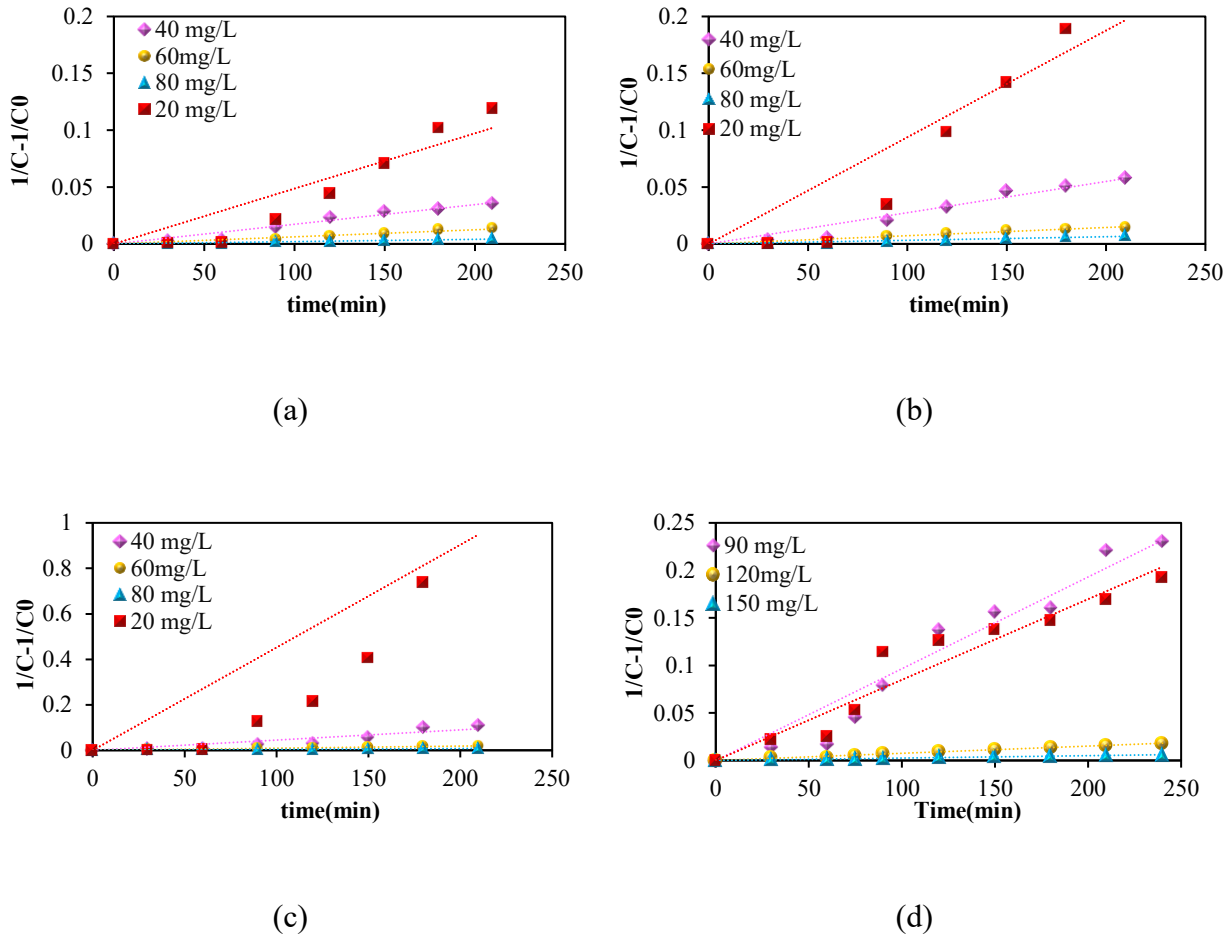


Fig. 18. Contaminant photocatalytic degradation kinetics (Second-order) using COF/HKUST/$CoFe_2O_4$-1 (a) COF/HKUST/$CoFe_2O_4$-2 (b) COF/HKUST/C $CoFe_2O_4$-3 (c) for MB, and COF/HKUST/ $CoFe_2O_4$ -3 (d) for DOX

3.2.6. Degradation mechanism

Developing heterojunction photocatalyst presents a promising strategy for achieving optimize excited charge carriers and minimize electron-hole recombination. The advanced solid-state Z-junction, comprised of two semiconductors and an electron mediator, has emerged as a prevalent configuration for such junctions. This Z-scheme concept draws inspiration from the

photosynthesis. In this mechanism, electrons generated by one semiconductor (HKUST) and holes produced by another (cobalt ferrite) are efficiently combined through the electron mediator (COF) when exposed to visible light. This process effectively inhibits charge carrier recombination, thereby preserving redox properties [52,53]. Often, carbon nanomaterials (CNMs) are used in heterogeneous junctions to improve the conductivity of semiconductor photocatalysts. In this context, COF has been selected as the electron mediator in the design of the photocatalyst [54]. The effect of active species generated during visible light irradiation on the photocatalysis process was investigated in three separate containers containing pollutant solution and photocatalyst. Following an initial adsorption-desorption equilibrium and an increase in hydrogen peroxide, various scavengers (EDTA, isopropyl alcohol, and ascorbic acid) were added before the containers were exposed to light irradiation.

Fig. 19 presented the proposed degradation mechanism of pollutant using COF/HKUST/$CoFe_2O_4$. To evaluate the photocatalytic mechanism of the synthesized composite, Mott-Schottky analysis was performed alongside DRS analysis. The energy levels of the synthesized materials were calculated based on these analyses. Based on these findings, a Z-scheme mechanism for pollutant degradation was proposed and is explained below. Irradiating a semiconductor with light of energy more than or equal to bandgap (energy ≥ bandgap) excites electrons from the valence band to the conduction band, creating holes in the valence band. Considering the band gaps of the composite components, all three semiconductors can absorb visible light, and the cobalt ferrite component has the narrowest band gap, allowing for broader absorption in the visible spectrum, so it can be a momentous part for visible light harvesting.

$$CoFe_2O_4\ (Eg = 1.6\ eV) + h\nu \rightarrow e^-_{CB} + h_{VB}^+ \quad (1)$$

$$COF\ (Eg = 2.11\ eV) + h\nu \rightarrow e^-_{CB} + h_{VB}^+ \quad (2)$$

HKUST (Eg =2.65 eV) + hν → e^-_{CB} + h_{VB}^+ (3)

COF component, with the most negative CB (-1.793 eV), is ideally suited for reducing O_2 to $\bullet O_2^-$. However, its VB (0.317 eV) is insufficient for oxidizing H_2O to •OH or directly oxidizing most pollutants. HKUST component has a VB (1.75 eV) suitable for oxidizing pollutants or H_2O_2 to •OH, and its CB (-0.9 eV) can reduce O_2 to $\bullet O_2^-$. $CoFe_2O_4$ component has a less negative CB (-0.158 eV), which limits its ability to reduce O_2. Its VB (1.442 eV) can perform some oxidation reactions, although it's less potent than HKUST. Given these energy positions, a Z-scheme configuration is likely, promoting efficient charge separation while retaining strong redox potentials [59,60]. Under visible light irradiation, all components (COF, HKUST, and $CoFe_2O_4$) absorb photons, leading to the excitation of electrons from the VB to the CB, leaving corresponding holes in the VB. Electrons in CB of $CoFe_2O_4$ recombine with holes in VB of COF at the interface due to their energetically close proximity. This leaves electrons in CB of COF and holes in VB of HKUST, effectively maximizing the redox potential of the composite material.

A recombination pathway involves electrons in CB of HKUST recombining with holes in VB of $CoFe_2O_4$, which would also leave electrons in COF's CB. However, holes would reside in VB of $CoFe_2O_4$. This configuration, with holes in VB of HKUST, is more favorable because VB of HKUST exhibits a stronger oxidation potential. This preferential configuration retains COF's strong reduction potential and HKUST's strong oxidation potential, optimizing the overall photocatalytic performance. Electrons in CB of COF (-1.793 eV) are highly reducing and react with O_2 to form superoxide radicals:

O_2+ e_{CB}^- → $\bullet O_2^-$(−0.33 eV vs. NHE) (4)

Holes in VB of HKUST (+1.75 eV) can oxidize pollutants directly or react with H_2O_2. Adding H_2O_2 significantly enhances photocatalysis by acting as an electron acceptor and a source of highly reactive •OH radicals. The effects of H_2O_2 include electron scavenging, where H_2O_2 accepts electrons from the conduction band (CB) of the COF (-1.793 eV), preventing electron-hole recombination. This process increases the availability of holes in the valence band (VB) of HKUST for oxidation.

$$H_2O_2 + h\nu \text{ (visible light)} \rightarrow \bullet OH + -OH \quad (5)$$

$$H_2O_2 + e_{CB}^- \rightarrow \bullet OH + OH^- \text{ (+0.32 eV vs. NHE)} \quad (6)$$

Hydrogen peroxide (H_2O_2) can be oxidized by photogenerated holes (h^+) in the valence band (VB) of HKUST, forming perhydroxyl radicals (•OOH) and protons (H^+). The •OOH radical can subsequently decompose to generate •OH or other reactive species.

$$H_2O_2 + h_{VB}^+ \rightarrow \bullet OOH + H^+ \quad (7)$$

The presence of H_2O_2 amplifies •OH production compared to direct H_2O oxidation. Direct water oxidation requires a high VB potential (> +2.31 eV), which is not attainable by either HKUST or $CoFe_2O_4$. H_2O_2 circumvents this limitation. Superoxide radicals ($\bullet O_2^-$) generated from the conduction band (CB) of the covalent organic framework (COF) can react with protons (H^+) to form H_2O_2, which further decomposes into •OH, establishing a self-sustaining ROS cycle:

$$\bullet O_2^- + 2H^+ + e^- \rightarrow H_2O_2 \quad (8)$$

$$H_2O_2 + e^- \rightarrow \bullet OH + OH^- \quad (9)$$

Photogenerated holes in the VB of HKUST directly oxidize pollutants or react with H_2O_2 to form •OH or •OOH. The •OH and $\bullet O_2^-$ radicals then attack the pollutants, breaking them down

into smaller fragments that are eventually mineralized to CO_2 and H_2O, and other products. Totally, the synergistic combination of the composite' components and the ability of H_2O_2 to produce Reactive species makes it a highly effective system for photocatalytic degradation of organic pollutants[61–63].

$$(DOX)/(MB) + \bullet O_2^-/OH/\ h^+_{VB} \rightarrow CO_2 + H_2O + \text{Other degradation Products} \quad (10)$$

Ascorbic acid, EDTA, and isopropyl alcohol functioned as peroxide, h^+, and hydroxyl radical scavengers, respectively, leading to pollutant degradation decreases of approximately 14.7%, 42.7%, and 24.6% (Fig. 20). Among these, EDTA had the most significant impact on degradation efficiency, while ascorbic acid only contributed to a competitive environment, showing minimal reduction in degradation. Overall, the importance of active species for DOX was determined to follow the order: h^+ > •OH > $\bullet O_2^-$. The same applies to methylene blue, where the order of active species is h^+ > •OH. Interestingly, ascorbic acid enhanced the degradation, achieving a higher rate than the sample without a scavenger [64,65].

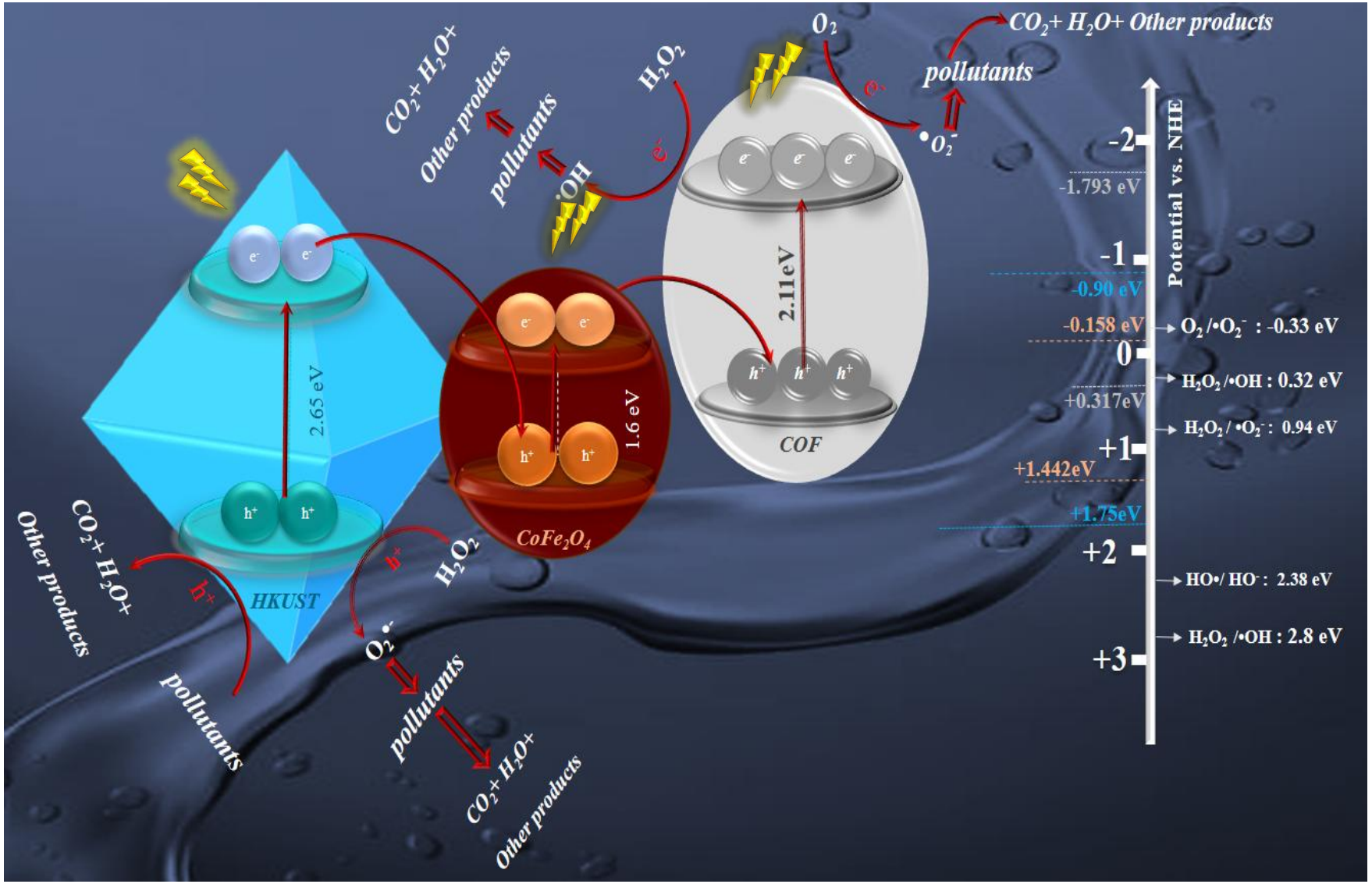
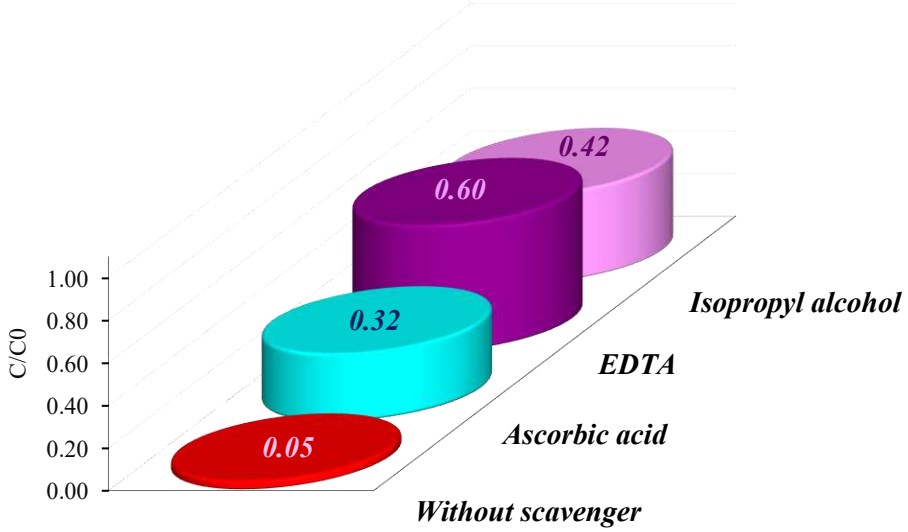
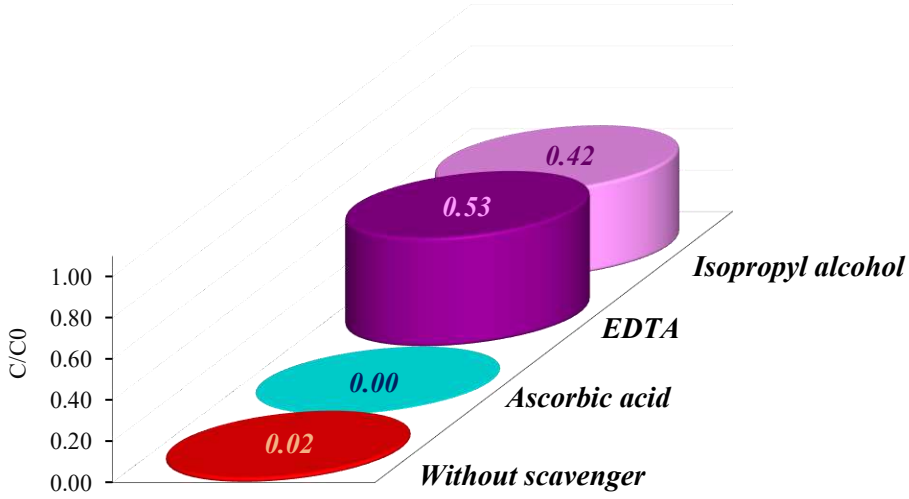


Fig. 19. The proposed degradation mechanism of pollutant using COF/HKUST/$CoFe_2O_4$.



(a)



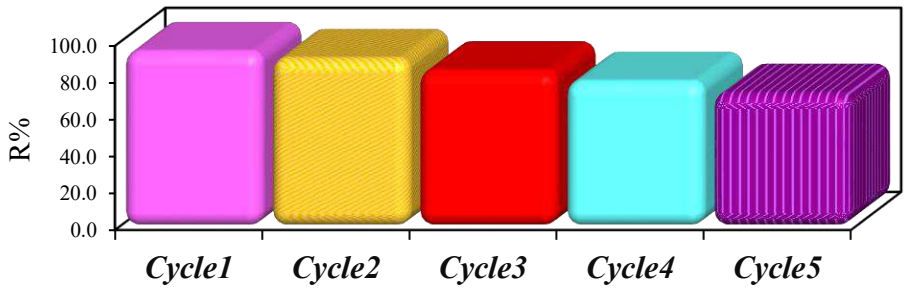
(b)

Fig. 20. Active species effect in the photocatalytic degradation of DOX (a), MB (b) utilizing COF/HKUST/$CoFe_2O_4$

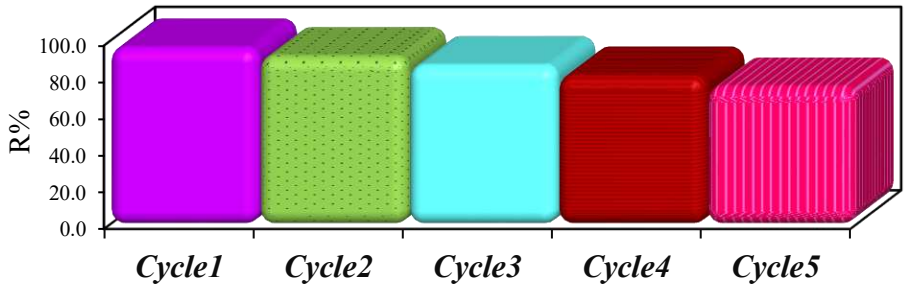
3.2.7. Reusability and stability

A key challenge in the design of new catalysts is ensuring their stability and efficiency after several uses in pollutant removal (Fig. 21). Researchers are exploring novel methods to enhance the

durability and activity of photocatalysts over several cycles, resulting in more effective and long-lasting materials. This not only lowers operational costs associated with catalysts but also minimizes waste from discarded materials, aligning with sustainability goals. Ultimately, this approach reduces environmental impacts, enhances economic benefits, improves efficiency, and fosters technological innovation. Degradation efficiency for DOX removal remained satisfactory after five recycling cycles, with results of 95.4%, 91.6%, 84.9%, 79.2%, and 72.7%, respectively. Methylene blue degradation of 97.5%, 92.3%, 87.4%, 81.7%, and 75.7% emphasizes the photocatalyst stability and performance [66–68].



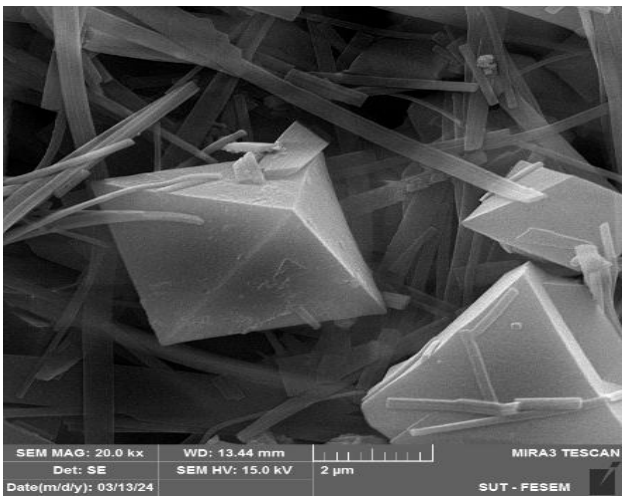
(a)



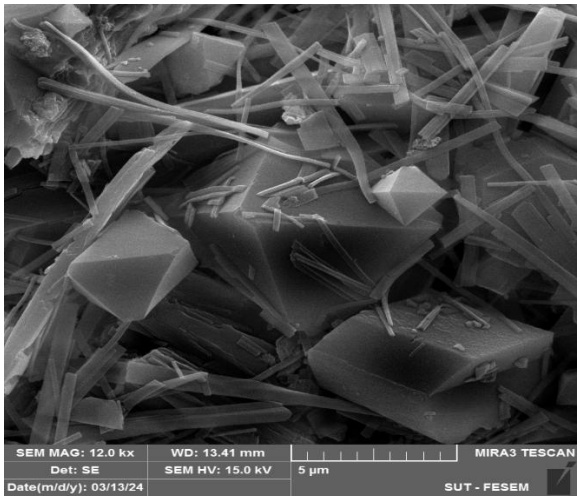
(b)

Fig. 21. Reusability of COF/HKUST/$CoFe_2O_4$ photocatalyst for contaminant degradation (a) DOX and (b) MB.

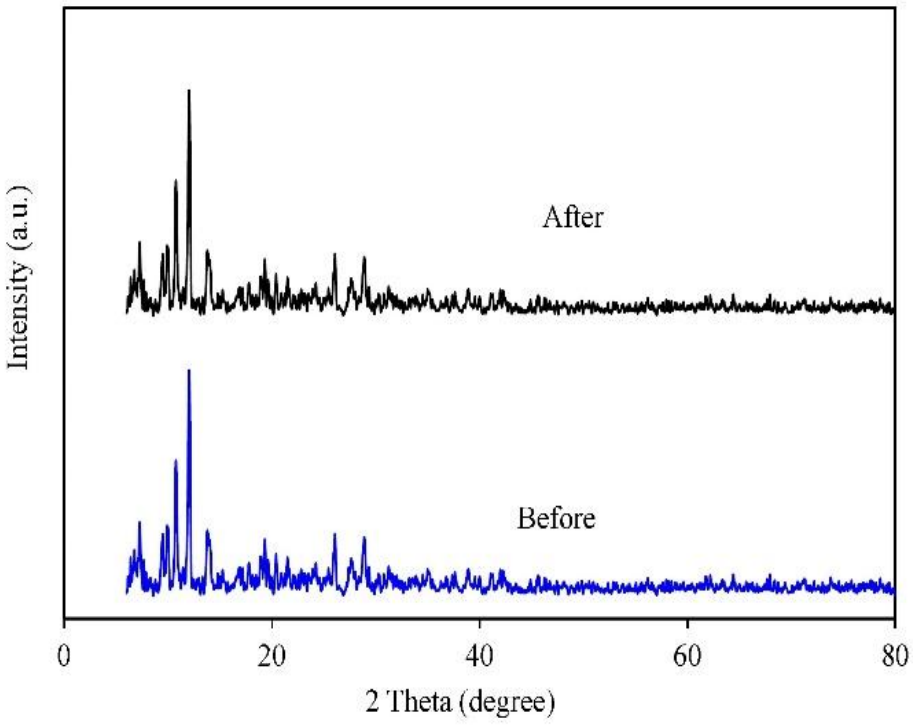
Fig. 22 presented the SEM images of COF/HKUST/$CoFe_2O_4$ before and after contaminant removal. They showed that the morphology of the COF/HKUST/$CoFe_2O_4$ did not change considerably before and after pollutant degradation because of its stability and reusability after five successive cycles. In addition, Fig. 22 presented the XRD patterns of COF/HKUST/$CoFe_2O_4$ before and after pollutant degradation. The results indicated that XRD patterns of COF/HKUST/$CoFe_2O_4$ did not changed considerably before and after pollutant degradation due to the stability of hybrid.



(a)



(b)



(c)

545 Fig. 22. SEM images ((a) before and (b) after) and (c) XRD patterns of hybrid before and after

546 pollutant degradation.

547

4. Conclusion

This study advances environmental remediation by designing a COF/HKUST/$CoFe_2O_4$ magnetic ternary composite via a green synthesis route using non-toxic solvents. The composite achieved 97% photocatalytic degradation of methylene blue (20 mg/L) and 95% for doxycycline (90 mg/L) under visible light, with facile magnetic recoverability enabling reuse. Enhanced performance arises from synergistic interactions among the dual organic frameworks and cobalt ferrite, including suppressed electron-hole recombination, π-π interactions, a narrowed band gap, and a novel three-component Z-scheme charge transfer pathway. Degradation followed first-order kinetics for methylene blue and second-order for doxycycline, with active species scavenging experiments identifying photogenerated holes h^+ > •OH as dominant contributors. Beyond advancing photocatalytic hybrid materials, this work integrates green chemistry principles to optimize composite architectures, offering scalable solutions for water pollution and sustainability challenges. These findings pave the way for next-generation, eco-friendly photocatalysts tailored to persistent organic contaminants.

Data availability

Data are available upon request from the authors

Conflicts of interest

No conflicts of interest

Funding declaration

'None'.

CRediT Author Statement

Bahareh Rabeie: Methodology, Software, Validation, Formal analysis, Investigation, Data Curation, Writing - Original Draft, Visualization.

Niyaz Mohammad Mahmoodi: Conceptualization, Methodology, Software, Validation, Formal analysis, Investigation, Resources, Data Curation, Writing - Original Draft, Writing - Review & Editing, Visualization, Supervision, Project administration, Funding acquisition

Hossein Kazemian:, Methodology, Software, Investigation, Resources, Data Curation, Writing - Original Draft, Writing - Review & Editing, Visualization, Supervision, Project administration

References

[1] Z. Yang, N. Wei, N. Xue, R. Xu, E. Yang, F. Wang, H. Zhu, H. Cui, Highly efficient MoS2/MXene aerogel for interfacial solar steam generation and wastewater treatment, J. Colloid Interface Sci. 656 (2024) 189–199. https://doi.org/10.1016/j.jcis.2023.11.110.

[2] Y. Sun, X. Meng, Y. Dall'Agnese, C. Dall'Agnese, S. Duan, Y. Gao, G. Chen, X.F. Wang, 2D MXenes as Co-catalysts in Photocatalysis: Synthetic Methods, Nano-Micro Lett. 11 (2019). https://doi.org/10.1007/s40820-019-0309-6.

[3] W.A. Thompson, E. Sanchez Fernandez, M.M. Maroto-Valer, Review and Analysis of CO 2 Photoreduction Kinetics , ACS Sustain. Chem. Eng. 8 (2020) 4677–4692. https://doi.org/10.1021/acssuschemeng.9b06170.

[4] V. Russo, M. Hmoudah, F. Broccoli, M.R. Iesce, Applications of Metal Organic Frameworks in Wastewater Treatment : A Review on Adsorption and Photodegradation, 2 (2020) 1–13. https://doi.org/10.3389/fceng.2020.581487.

[5] S. Mishra, B. Sundaram, A review of the photocatalysis process used for wastewater treatment, Mater. Today Proc. (2023). https://doi.org/10.1016/J.MATPR.2023.07.147.

[6] X. Tao, Y. Zhao, S. Wang, C. Li, R. Li, Recent advances and perspectives for solar-driven water splitting using particulate photocatalysts (Chem. Soc. Rev. (2022) 51 (3561-3608) DOI: 10.1039/d1cs01182k), Chem. Soc. Rev. 51 (2022) 10120–10122. https://doi.org/10.1039/d2cs90098j.

[7] X. Chen, X. Peng, L. Jiang, X. Yuan, J. Fei, W. Zhang, Photocatalytic removal of antibiotics by MOF-derived Ti3+- and oxygen vacancy-doped anatase/rutile TiO2 distributed in a carbon matrix, Chem. Eng. J. 427 (2022) 130945. https://doi.org/10.1016/j.cej.2021.130945.

[8] R. Daghrir, P. Drogui, Tetracycline antibiotics in the environment: A review, Environ. Chem. Lett. 11 (2013) 209–227. https://doi.org/10.1007/s10311-013-0404-8.

[9] C. Yang, Y. Zhu, J. Wang, W. Sun, L. Yang, H. Lin, S. Lv, A novel granular MOF composite with dense and ordered MIL-100(Fe) nanoparticles grown on porous alumina: Green synthesis and enhanced adsorption of tetracycline hydrochloride, Chem. Eng. J. 426 (2021) 131724. https://doi.org/10.1016/j.cej.2021.131724.

[10] I. Khan, K. Saeed, I. Zekker, B. Zhang, A.H. Hendi, A. Ahmad, S. Ahmad, N. Zada, H. Ahmad, L.A. Shah, T. Shah, I. Khan, and Photodegradation, (2022).

[11] F. Ahmadijokani, A. Ghaffarkhah, H. Molavi, S. Dutta, Y. Lu, S. Wuttke, M. Kamkar, O.J. Rojas, M. Arjmand, COF and MOF Hybrids: Advanced Materials for Wastewater Treatment, Adv. Funct. Mater. 2305527 (2023). https://doi.org/10.1002/adfm.202305527.

[12] R. Freund, O. Zaremba, G. Arnauts, R. Ameloot, G. Skorupskii, M. Dincă, A. Bavykina, J. Gascon, A. Ejsmont, J. Goscianska, M. Kalmutzki, U. Lächelt, E. Ploetz, C.S. Diercks, S. Wuttke, The Current Status of MOF and COF Applications, Angew. Chemie - Int. Ed. 60 (2021) 23975–24001. https://doi.org/10.1002/anie.202106259.

[13] S.W. Lv, J.M. Liu, Z.H. Wang, H. Ma, C.Y. Li, N. Zhao, S. Wang, Recent advances on porous organic frameworks for the adsorptive removal of hazardous materials, J. Environ. Sci. (China). 80 (2019) 169–185. https://doi.org/10.1016/j.jes.2018.12.010.

[14] T. Luo, L. Gilmanova, S. Kaskel, Advances of MOFs and COFs for photocatalytic CO2 reduction, H2 evolution and organic redox transformations, Coord. Chem. Rev. 490

(2023) 215210. https://doi.org/10.1016/j.ccr.2023.215210.

[15] S. Zhou, Y. Kuang, H. Yang, L. Gan, X. Feng, C. Mao, L. Chen, J. Zheng, G. Ouyang, S. Zhou, Y. Kuang, H. Yang, L. Gan, X. Feng, Supporting Information Structure-Controlled Interpenetrated MOF @ COF via C À C Linkage for Enhanced Photocatalysis for Enhanced Photocatalysis, (n.d.).

[16] H. Wang, X. Li, X. Zhao, C. Li, X. Song, P. Zhang, P. Huo, A review on heterogeneous photocatalysis for environmental remediation: From semiconductors to modification strategies, Chinese J. Catal. 43 (2022) 178–214. https://doi.org/10.1016/S1872-2067(21)63910-4.

[17] A. Balapure, J. Ray Dutta, R. Ganesan, Recent advances in semiconductor heterojunctions: a detailed review of the fundamentals of photocatalysis, charge transfer mechanism and materials, RSC Appl. Interfaces. 1 (2024) 43–69. https://doi.org/10.1039/d3lf00126a.

[18] R. Long, Z. Yu, Q. Tan, X. Feng, X. Zhu, X. Li, P. Wang, Ti3C2 MXene/NH2-MIL-88B(Fe): Research on the adsorption kinetics and photocatalytic performance of an efficient integrated photocatalytic adsorbent, Appl. Surf. Sci. 570 (2021). https://doi.org/10.1016/j.apsusc.2021.151244.

[19] S. Salehian, A. Larimi, A.A. Asgharinezhad, N. Khallaghi, T.N. Borhani, C. Ghotbi, Magnetic Z-scheme bismuth molybdate(1-x)/Fe3O4@MIL-125(Ti)(x) nanocomposite as a high-performance visible-light-active photocatalyst for ultra-deep oxidative desulfurization of liquid fuel, Surfaces and Interfaces. 42 (2023). https://doi.org/10.1016/j.surfin.2023.103432.

[20] Y. Li, W. Chen, R. Gao, Z. Zhao, T. Zhang, G. Xing, L. Chen, 2D covalent organic frameworks with built-in amide active sites for efficient heterogeneous catalysis, Chem. Commun. 55 (2019) 14538–14541. https://doi.org/10.1039/c9cc07500c.

[21] A. V. Ravindra, M. Chandrika, C. Rajesh, P. Kollu, S. Ju, S.D. Ramarao, Simple synthesis, structural and optical properties of cobalt ferrite nanoparticles, Eur. Phys. J. Plus. 134 (2019). https://doi.org/10.1140/epjp/i2019-12690-2.

[22] P.S.S.R. Gibin, Preparation and characterization of nanosized cobalt ferrite particles by co-precipitation method with citrate as chelating agent, J. Mater. Sci. Mater. Electron. 27 (2016) 8891–8898. https://doi.org/10.1007/s10854-016-4915-5.

[23] L. Cui, P. Guo, G. Zhang, Q. Li, R. Wang, M. Zhou, L. Ran, X.S. Zhao, Facile synthesis of cobalt ferrite submicrospheres with tunable magnetic and electrocatalytic properties, Colloids Surfaces A Physicochem. Eng. Asp. 423 (2013) 170–177. https://doi.org/10.1016/j.colsurfa.2013.01.064.

[24] L. Shao, M. Liu, Y. Sang, J. Huang, One-pot synthesis of melamine-based porous polyamides for CO2 capture, Microporous Mesoporous Mater. 285 (2019) 105–111. https://doi.org/10.1016/j.micromeso.2019.05.005.

[25] M. Sarabaegi, M. Roushani, H. Hosseini, S.J. Hoseini, M. Bahrami, Facile synthesis of a covalent organic framework (COF) based on the reaction of melamine and trimesic acid incorporated electrospun nanofiber and its application as an electrochemical tyrosinamide aptasensor, New J. Chem. 44 (2020) 14922–14927. https://doi.org/10.1039/d0nj02837a.

[26] S. Zulfiqar, M.I. Sarwar, C.T. Yavuz, Melamine based porous organic amide polymers for CO2 capture, RSC Adv. 4 (2014) 52263–52269. https://doi.org/10.1039/c4ra11442f.

[27] K. Schlichte, T. Kratzke, S. Kaskel, Improved synthesis, thermal stability and catalytic properties of the metal-organic framework compound Cu3(BTC)2, Microporous Mesoporous Mater. 73 (2004) 81–88. https://doi.org/10.1016/j.micromeso.2003.12.027.

[28] S.B. Bagherzadeh, M. Kazemeini, N.M. Mahmoodi, A study of the DR23 dye photocatalytic degradation utilizing a magnetic hybrid nanocomposite of MIL-53(Fe)/CoFe2O4: Facile synthesis and kinetic investigations, J. Mol. Liq. 301 (2020) 112427. https://doi.org/10.1016/j.molliq.2019.112427.

[29] R. Peymanfar, F. Azadi, Y. Yassi, Preparation and Characterization of CuFe 2 O 4 Nanoparticles by the Sol-Gel Method and Investigation of its Microwave Absorption Properties at Ku-band Frequency using Silicone Rubber, (2018) 2–7.

[30] T. Amuthan, R. Sanjeevi, G.R. Kannan, A. Sridevi, Physica B : Physics of Condensed Matter A novel p-CuFe 2 O 4 / n-ZnS heterojunction photocatalyst : Co-precipitation

synthesis , characterization and improved visible-light driven photocatalytic activity for removal of MB and CV dyes, Phys. B Phys. Condens. Matter. 638 (2022) 413842. https://doi.org/10.1016/j.physb.2022.413842.

[31] E. Hutamaningtyas, Utari, Suharyana, A.T. Wijayanta, B. Purnama, FTIR and structural properties of co-precipitated cobalt ferrite nano particles, J. Phys. Conf. Ser. 776 (2016). https://doi.org/10.1088/1742-6596/776/1/012023.

[32] C. Cai, X. Fan, X. Han, J. Li, H. Vardhan, Improved Desulfurization Performance of Polyethyleneglycol Membrane by Incorporating Metal Organic Framework CuBTC, (2020). https://doi.org/10.3390/polym12020414.

[33] J.Y. Lee, Copper-based metal-organic framework for highly ef fi cient adsorption of lead ions from aqueous solution, Mater. Res. Express. 9 (2022) 95505. https://doi.org/10.1088/2053-1591/ac93ea.

[34] M.G. Mohamed, S.U. Sharma, N.Y. Liu, T.H. Mansoure, M.M. Samy, S. V. Chaganti, Y.L. Chang, J.T. Lee, S.W. Kuo, Ultrastable Covalent Triazine Organic Framework Based on Anthracene Moiety as Platform for High-Performance Carbon Dioxide Adsorption and Supercapacitors, Int. J. Mol. Sci. 23 (2022). https://doi.org/10.3390/ijms23063174.

[35] S.O. Akinnawo, Covalent organic frameworks: Design, synthesis, characterization, and applications, ChemPhysMater. 3 (2023) 36–63. https://doi.org/10.1016/j.chphma.2023.08.003.

[36] M. Mehta, R. Naffa, C. Maidment, G. Holmes, M. Waterland, Raman and Atr-Ftir Spectroscopy Towards Classification of Wet Blue Bovine Leather Using Ratiometric and Chemometric Analysis, J. Leather Sci. Eng. 2 (2020). https://doi.org/10.1186/s42825-019-0017-5.

[37] M. Guo, M. Lu, H. Zhao, F. Lin, F. He, J. Zhang, S. Wang, P. Dong, C. Zhao, Efficient electro-Fenton catalysis by self-supported CFP@CoFe2O4 electrode, J. Hazard. Mater. 423 (2022) 127033. https://doi.org/10.1016/j.jhazmat.2021.127033.

[38] C. Suwanchawalit, V. Somjit, Hydrothermal synthesis of magnetic CoFe2O4-graphene nanocomposite with enhanced photocatalytic performance, Dig. J. Nanomater.

Biostructures. 10 (2015) 769–777.

[39] Y. Mao, W. Cao, J. Li, Y. Liu, Y. Ying, L. Sun, X. Peng, Enhanced gas separation through well-intergrown MOF membranes: Seed morphology and crystal growth effects, J. Mater. Chem. A. 1 (2013) 11711–11716. https://doi.org/10.1039/c3ta12402a.

[40] A. Yang, P. Li, J. Zhong, Facile preparation of low-cost HKUST-1 with lattice vacancies and high-efficiency adsorption for uranium, RSC Adv. 9 (2019) 10320–10325. https://doi.org/10.1039/c9ra01427f.

[41] J.K. Rajput, G. Kaur, Synthesis and applications of CoFe2O4 nanoparticles for multicomponent reactions, Catal. Sci. Technol. 4 (2014) 142–151. https://doi.org/10.1039/c3cy00594a.

[42] S.V. Elanthamilan, E. Princy, M. Johnson, I.S. Lydia, Multifunctional magnetic - CoFe 2 O 4 nanoparticles for the photocatalytic discoloration of aqueous methyl violet dye and energy storage applications, J. Mater. Sci. Mater. Electron. (2020). https://doi.org/10.1007/s10854-020-03624-z.

[43] H. Bin Wu, B.Y. Xia, L. Yu, X.Y. Yu, X.W. Lou, Porous molybdenum carbide nano-octahedrons synthesized via confined carburization in metal-organic frameworks for efficient hydrogen production, Nat. Commun. 6 (2015) 1–8. https://doi.org/10.1038/ncomms7512.

[44] H. Lu, L. Zhang, B. Wang, Y. Long, M. Zhang, J. Ma, A. Khan, S.P. Chowdhury, X. Zhou, Y. Ni, Cellulose-supported magnetic Fe3O4–MOF composites for enhanced dye removal application, Cellulose. 26 (2019) 4909–4920. https://doi.org/10.1007/s10570-019-02415-y.

[45] W. Zhu, X. Li, Y. Sun, R. Guo, S. Ding, Introducing hydrophilic ultra-thin ZIF-L into mixed matrix membranes for CO2/CH4 separation, RSC Adv. 9 (2019) 23390–23399. https://doi.org/10.1039/c9ra04147h.

[46] S. Ahmadian-Fard-Fini, M. Salavati-Niasari, H. Safardoust-Hojaghan, Hydrothermal green synthesis and photocatalytic activity of magnetic CoFe2O4–carbon quantum dots nanocomposite by turmeric precursor, J. Mater. Sci. Mater. Electron. 28 (2017) 16205–

16214. https://doi.org/10.1007/s10854-017-7522-1.

[47] X. Yang, Z. Guo, X. Chen, S. Xi, K. Cui, J. Li, D. Dong, F. Wu, Z. Wu, Efficient degradation of thiamethoxam pesticide in water by iron and manganese oxide composite biochar activated persulfate, Chem. Eng. J. 473 (2023) 145051. https://doi.org/10.1016/j.cej.2023.145051.

[48] J. Ma, Y. Xiao, J. Chen, Y. Shen, S. Xiao, S. Cao, Dual-pathway charge transfer mechanism of anatase/rutile TiO2-Ag3PO4 hollow photocatalyst promotes efficient degradation of pesticides, J. Colloid Interface Sci. 678 (2025) 334–344. https://doi.org/10.1016/j.jcis.2024.08.162.

[49] V. Russo, M. Hmoudah, F. Broccoli, M.R. Iesce, O.-S. Jung, M. Di Serio, Applications of Metal Organic Frameworks in Wastewater Treatment: A Review on Adsorption and Photodegradation, Front. Chem. Eng. 2 (2020). https://doi.org/10.3389/fceng.2020.581487.

[50] G. Singh, M.K. Ubhi, K. Jeet, C. Singla, M. Kaur, A Review on Impacting Parameters for Photocatalytic Degradation of Organic Effluents by Ferrites and Their Nanocomposites, Processes. 11 (2023) 1727. https://doi.org/10.3390/pr11061727.

[51] H.D. Tran, D.Q. Nguyen, P.T. Do, U.N.P. Tran, Kinetics of photocatalytic degradation of organic compounds: a mini-review and new approach, RSC Adv. 13 (2023) 16915–16925. https://doi.org/10.1039/d3ra01970e.

[52] N. Syed, J. Huang, Y. Feng, X. Wang, L. Cao, Carbon-Based Nanomaterials via Heterojunction Serving as Photocatalyst, Front. Chem. 7 (2019) 1–7. https://doi.org/10.3389/fchem.2019.00713.

[53] S. Junwang, Visible-light driven heterojunction photocatalysts for water splitting – a critical review, Energy Environ. Sci. 8 (2015) 731–759. https://doi.org/10.1039/C4EE03271C.

[54] T.S. Natarajan, K.R. Thampi, R.J. Tayade, Visible light driven redox-mediator-free dual semiconductor photocatalytic systems for pollutant degradation and the ambiguity in applying Z-scheme concept, Appl. Catal. B Environ. 227 (2018) 296–311.

https://doi.org/10.1016/j.apcatb.2018.01.015.

[55] Y. Ma, Q. Wang, S. Xing, Insight into the catalytic mechanism of γ-Fe2O3/ZnFe2O4 for hydrogen peroxide activation under visible light, J. Colloid Interface Sci. 529 (2018) 247–254. https://doi.org/10.1016/j.jcis.2018.06.020.

[56] S. Behnam, M. Kazemeini, N. Mohammad, Journal of Colloid and Interface Science Preparation of novel and highly active magnetic ternary structures (metal-organic framework / cobalt ferrite / graphene oxide) for effective visible-light-driven photocatalytic and photo-Fenton-like degradation o, J. Colloid Interface Sci. 602 (2021) 73–94. https://doi.org/10.1016/j.jcis.2021.05.181.

[57] Y. Yang, S. Ma, J. Qu, J. Li, Y. Liu, Q. Wang, J. Jing, Y. Yuan, T. Yao, J. Wu, Transforming type-II Fe2O3@polypyrrole to Z-scheme Fe2O3@polypyrrole/Prussian blue via Prussian blue as bridge: Enhanced activity in photo-Fenton reaction and mechanism insight, J. Hazard. Mater. 405 (2021) 124668. https://doi.org/10.1016/j.jhazmat.2020.124668.

[58] M. Fattahi, Z. Niazi, F. Esmaeili, A.A. Mohammadi, M. Shams, B. Nguyen Le, Boosting the adsorptive and photocatalytic performance of MIL-101(Fe) against methylene blue dye through a thermal post-synthesis modification, Sci. Rep. 13 (2023) 1–13. https://doi.org/10.1038/s41598-023-41451-4.

[59] J.H. Shah, M. Fiaz, M. Athar, J. Ali, M. Rubab, R. Mehmood, S.U.U. Jamil, R. Djellabi, Facile synthesis of N/B-double-doped Mn2O3 and WO3 nanoparticles for dye degradation under visible light, Environ. Technol. (United Kingdom). 41 (2020) 2372–2381. https://doi.org/10.1080/09593330.2019.1567604.

[60] S.S. Mukonza, N. Chaukura, A.K. Mishra, Photocatalytic Activity and Reusability of F, Sm3+ Co-Doped TiO2/MWCNTs Hybrid Heterostructure for Efficient Photocatalytic Degradation of Brilliant Black Bis-Azo Dye, Catalysts. 13 (2023) 1–18. https://doi.org/10.3390/catal13010086.

[61] L. Thi Thanh Nhi, L. Van Thuan, D. My Uyen, M.H. Nguyen, V.T. Thu, D.Q. Khieu, L.H. Sinh, Facile fabrication of highly flexible and floatable Cu2O/rGO on Vietnamese

traditional paper toward high-performance solar-light-driven photocatalytic degradation of ciprofloxacin antibiotic, RSC Adv. 10 (2020) 16330–16338. https://doi.org/10.1039/d0ra01854f.

[62] M. Ikram, S. Aslam, A. Haider, S. Naz, A. Ul-Hamid, A. Shahzadi, M. Ikram, J. Haider, S.O.A. Ahmad, A.R. Butt, Doping of Mg on ZnO Nanorods Demonstrated Improved Photocatalytic Degradation and Antimicrobial Potential with Molecular Docking Analysis, Nanoscale Res. Lett. 16 (2021). https://doi.org/10.1186/s11671-021-03537-8.

Supplementary Files

This is a list of supplementary files associated with this preprint. Click to download.

- Supplementaryfile.docx